Evaluation of Soil–Structure Interface Models

Hai-Lin Wang[1]; Zhen-Yu Yin[2]; Yin-Fu Jin[3]; and Xiao-Qiang Gu[4]

Abstract: Modeling of the soil–structure interface has been a critical issue in geotechnical engineering. Numerous studies have simulated complex soil–structure interface behaviors. These models usually are assessed by direct comparisons between the simulations and experiments. However, little work has been done to compare the specific interface behaviors simulated by different interface models. This paper evaluated some frequently recognized interface behaviors for six different interface models. These models either were adopted from the existing literature or modified from the existing soil models, including the exponential model, hyperbolic model, hypoplastic model, MCC model, SANISAND model, and SIMSAND model. Global comparisons and effects of the soil density, normal stiffness, and shearing rate were investigated to evaluate the interface models based on Fontainebleau sand–steel interface experiments and kaolin clay–steel interface experiments. The limitations and advantages of different models under different conditions were discussed. **DOI: 10.1061/JGGEFK.GTENG-11486.**

Author keywords: Soil–structure interface; Constitutive model; Parameter identification; Elastoplasticity; Model evaluation.

Introduction

The characterization of the soil–structure interface (SSI) has been a critical issue in geotechnical engineering, such as soil anchors, suction caissons, pile foundations, tunnels, and retaining walls. To investigate the behaviors of SSI, direct shear tests (Potyondy 1961; Littleton 1976; DeJong and Westgate 2009), simple shear tests (Uesugi and Kishida 1986; Kishida and Uesugi 1987; Fakharian and Evgin 2000), ring torsion shear tests (Yoshimi and Kishida 1981; Yasufuku and Ochiai 2005), annular shear tests (Brumund and Leonards 1973; Koval et al. 2011), cyclic interface shear test (CIST) (Qamar and Suleiman 2023), cyclic multiple-degree-of-free (CYMDOF) devices (Desai et al. 1985; Desai and Rigby 1997), cyclic three-dimensional simple shear interface (C3DSSI) tests (Fakharian and Evgin 1997), and large-scale shear tests (CSASSI) (Zhang and Zhang 2006) have been conducted. Based on these experiments, researchers have determined that a contact zone between the soil and the structure, the so-called soil–structure interface, is the key part of the whole system to transfer loads that connects the soil and the structure, within which the deformation and stress mainly take place when external forces are applied (Hu and Pu 2004; Pra-Ai 2013). Several key aspects that influence the interface behaviors have been investigated, such as the surface roughness (Potyondy 1961; Uesugi and Kishida 1986; DeJong and Westgate 2009), particle size and angularity (Potyondy 1961; Zhou and Yin 2023), relative density (Desai et al. 1985; DeJong and Westgate 2009; Taha and Fall 2013; Gu et al. 2017), confining normal stress and stiffness (Wernick 1978; Martinez and Frost 2017), rate effects (Tsubakihara and Kishida 1993; Lemos and Vaughan 2000; Martinez and Stutz 2019), and so forth. To simulate these soil–structure interface behaviors, numerous models have been proposed, such as the exponential model (Yang and Yin 2021), hyperbolic model (Clough and Duncan 1971), hypoplastic model (Arnold and Herle 2006; Stutz et al. 2016), and elastoplastic models (Desai and Ma 1992; Mortara 2001; Hu and Pu 2004; Lashkari 2013). These models usually are assessed by direct comparisons between the simulations and experiments, or by some statistical methods such as sensitivity study or uncertainty analysis (Stutz et al. 2015; Stutz 2016). This method guarantees the models' abilities to simulate the interface behaviors in a global sense. However, a model may have limitations in simulating specific behaviors, such as the density effects or rate effects. However, little work (Duque et al. 2022; Stutz et al. 2015) has been done to compare the specific behaviors simulated by different soil–structure interface models. Therefore, this paper evaluated some of these interface models in terms of some frequently recognized behaviors, to guide users to select a suitable model to be used in specific conditions.

This paper does not aim to propose a set of new interface models. The models used in this study either were adopted from the existing interface models or directly modified from the soil models following the general approach of applying existing soil models to simulate soil–structure interfaces (Stutz 2016; Staubach et al. 2022b). Simple nonlinear elastic models and complex elastoplastic models were selected for the comparison of these two groups of models. Six models were evaluated in this study: three simple nonlinear elastic models, and three elastoplastic models. First, the nonlinear exponential model was adopted from Yang et al. (2021) directly. Following the framework of the exponential model, the hyperbolic model is proposed by modifying the exponential function to a hyperbolic function, which has been used to simulate the interfaces (Clough and Duncan 1971). Then, the hypoplastic interface model is proposed by modifying the hypoplastic soil model proposed by Wang et al. (2018). Existing elastoplastic soil models then were modified to establish the elastoplastic interface models, including the MCC model modified from Roscoe and Burland (1968),

[1]Ph.D. Candidate, Dept. of Civil and Environmental Engineering, The Hong Kong Polytechnic Univ., Hong Kong 999077, China; Ph.D. Candidate, Dept. of Geotechnical Engineering, College of Civil Engineering, Tongji Univ., Shanghai 200092, China. Email: hailin.wang@connect.polyu.hk

[2]Professor, Dept. of Civil and Environmental Engineering, The Hong Kong Polytechnic Univ., Hong Kong 999077, China (corresponding author). Email: zhenyu.yin@polyu.edu.hk

[3]Professor, College of Civil and Transportation Engineering, Shenzhen Univ., Shenzhen 518060, China. Email: yinfujin@szu.edu.cn

[4]Professor, Dept. of Geotechnical Engineering, College of Civil Engineering, Tongji Univ., Shanghai 200092, China. Email: guxiaoqiang@tongji.edu.cn

Note. This manuscript was submitted on November 12, 2022; approved on January 19, 2024; published online on April 24, 2024. Discussion period open until September 24, 2024; separate discussions must be submitted for individual papers. This paper is part of the ***Journal of Geotechnical and Geoenvironmental Engineering***, © ASCE, ISSN 1090-0241.

the SANISAND model modified from Taiebat and Dafalias (2008), and the SIMSAND model modified from Yin et al. (2016). The proposed models focus on the simulation of the sand–structure interface. These models can be applied to both sand– and clay–structure interface experiments. However, simulations of the clay–structure interface have not been deeply investigated. These models were evaluated to identify the models' capabilities in simulating the interface behaviors, including global comparison, effects of the soil density, normal stiffness, and rate effect. The effects for different models were compared to identify the limitations and advantages for different models under different conditions, which should provide insights into selecting models under specific conditions.

Modeling Framework for the Soil–Structure Interface

A unified theoretical framework is presented to simplify the development of the SSI models so that different models can be consistent with the basic principle in nature. The interface is a thin layer of soil on the structure [Fig. 1(a)]. To investigate the SSI behavior, the direct shear SSI test often is conducted under three different boundary conditions [Fig. 1(b)].

The thickness of the interface is a key feature that should be considered to model SSI behaviors (Hu and Pu 2004; Tovar-Valencia et al. 2018). It has been widely recognized that the interface thickness can be considered to be several times the mean soil-particle diameter. Usually, the interface thickness is considered to be in the range of 5–14 times the mean particle diameter for the sand–structure interface (Uesugi and Kishida 1986; Hu and Pu 2004; Martinez and Frost 2017; Tovar-Valencia et al. 2018). For the clay–structure interface, the shear band thickness is much larger than the sand–structure interface reported in the literature (Martinez and Stutz 2019; Yavari et al. 2016). For example, Martinez and Stutz (2019) conducted kaolin clay–steel interface experiments and found out that the shear band thickness is 0.55 mm for rough surfaces and 0.27 mm for medium-rough surfaces (d_{50} is unknown; 52% of particle diameters are less than 2 μm, and therefore d_{50} should be less than 2 μm); Yavari et al. (2016) found the thickness to be less than 1 mm in kaolin clay–steel interface experiments with d_{50} equal to 0.8 μm. If we take the interface thickness divided by the mean particle diameter as an unknown variable, the interface thickness for sand can be expressed as

$$d_s = R_d \times d_{50} \qquad (R_d = d_s/d_{50} \approx 5\text{–}14) \tag{1}$$

For the clay–structure interface, because the particles have platy shapes, the deformation mechanism is different from the sand–structure interface, and the interface thickness usually is not assumed to be multiple times the d_{50} value (Yin et al. 2021). For interface tests under high-stress levels or large deformation, the shear band may exceed the interface thickness. For example, Ho et al. (2011) conducted large-deformation interface tests and found that the interface shear band was as much as 8 m. In this case, the soil tends to be crushed, and the shearing is concentrated in a thinner interface of the crushed soil. Thus, the interface thickness assumption is still valid. The relationship between the displacement and strain can be expressed as $\boldsymbol{\varepsilon} = \boldsymbol{u}/d_s$.

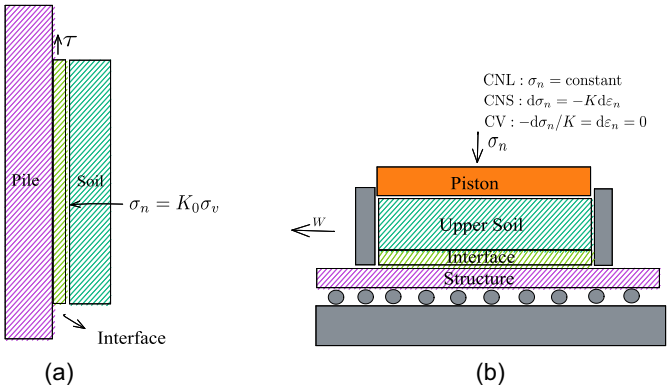

Fig. 1. Soil–structure interface: (a) in situ scale; and (b) laboratory scale.

The normal behavior of SSI often is represented by an elastic spring [Fig. 1(b)]. Depending on the stiffness of the interface, the interface tests can be divided into three different types (Potyondy 1961; Littleton 1976; Wernick 1978; Uesugi et al. 1988; Di Donna et al. 2016):

- Constant normal load (CNL): The normal load remains constant during the shearing, $d\sigma_n = 0$, implying $K = 0$.
- Constant normal stiffness (CNS): The relationship between the incremental normal stress and incremental normal strain is idealized by an elastic spring with a stiffness equal to K, which was introduced by Wernick (1978).
- Constant volume (CV): The volume of the soil remains constant during the shearing. Di Donna et al. (2016) called this boundary condition the constant normal height (CNH) condition. That is, no normal displacement is generated during the shearing, $d\varepsilon_n = 0$, implying $K = \infty$. The normal stress increment is not zero due to the constraint of the normal boundary. As discussed by Stutz (2016), it is challenging to satisfy this boundary condition due to the contractive behavior of loose sand, which leads to a reduction in volume of the interface by causing the soil to separate from the structure. Thus, we should be very careful when applying this boundary condition in the numerical simulation.

All three types of tests can be represented by the interface stiffness

$$d\sigma_n = -Kdu_n = -K'd\varepsilon_n \tag{2}$$

where du_n = incremental normal displacement; and $K' = Kd_s$ = modified stiffness, which takes the same unit as the stress.

Similar to the classical elastoplastic soil model, in the incremental form, a SSI model should be able to describe the relationship between the incremental stress $d\boldsymbol{\sigma}$ and the incremental strain $d\boldsymbol{\varepsilon}$

$$d\boldsymbol{\sigma} = \mathbf{D}(d\boldsymbol{\varepsilon} - d\boldsymbol{\varepsilon}^p) = \mathbf{D}d\boldsymbol{\varepsilon}^e = \mathrm{diag}([K_n, G, G])d\boldsymbol{\varepsilon}^e \tag{3}$$

where $\mathbf{D}$ is the stiffness matrix; and K_n and G = normal and shear stiffness, respectively. For nonlinear incremental SSI models, the plastic strain $d\boldsymbol{\varepsilon}^p$ is ignored, and the stiffness matrix $\mathbf{D}$ is assumed to be nonlinear according to the specific equations adopted. Similar to soil models, the integration of elastoplastic interface models is presented in the literature (e.g., Stutz et al. 2017; Staubach et al. 2022b). Generally, a SSI model should be able to describe the normal and tangential behaviors of the interface. The tangential behavior is represented by the relationship between the shear stress τ and the shear strain γ, whereas the normal behavior is represented by the relationship between the normal stress and normal strain. Combining Eqs. (2) and (3), the normal strain $d\varepsilon_n$ should be constrained by the following equation:

$$\begin{matrix} d\sigma_n = K_n(d\varepsilon_n - d\varepsilon_n^p) \\ d\sigma_n = -K'd\varepsilon_n \end{matrix} \Rightarrow d\varepsilon_n = \frac{K_n}{K_n + K'}d\varepsilon_n^p \tag{4}$$

Considering the consistency condition of the yield surface that guarantees that the stress state is always on the yield surface during the loading

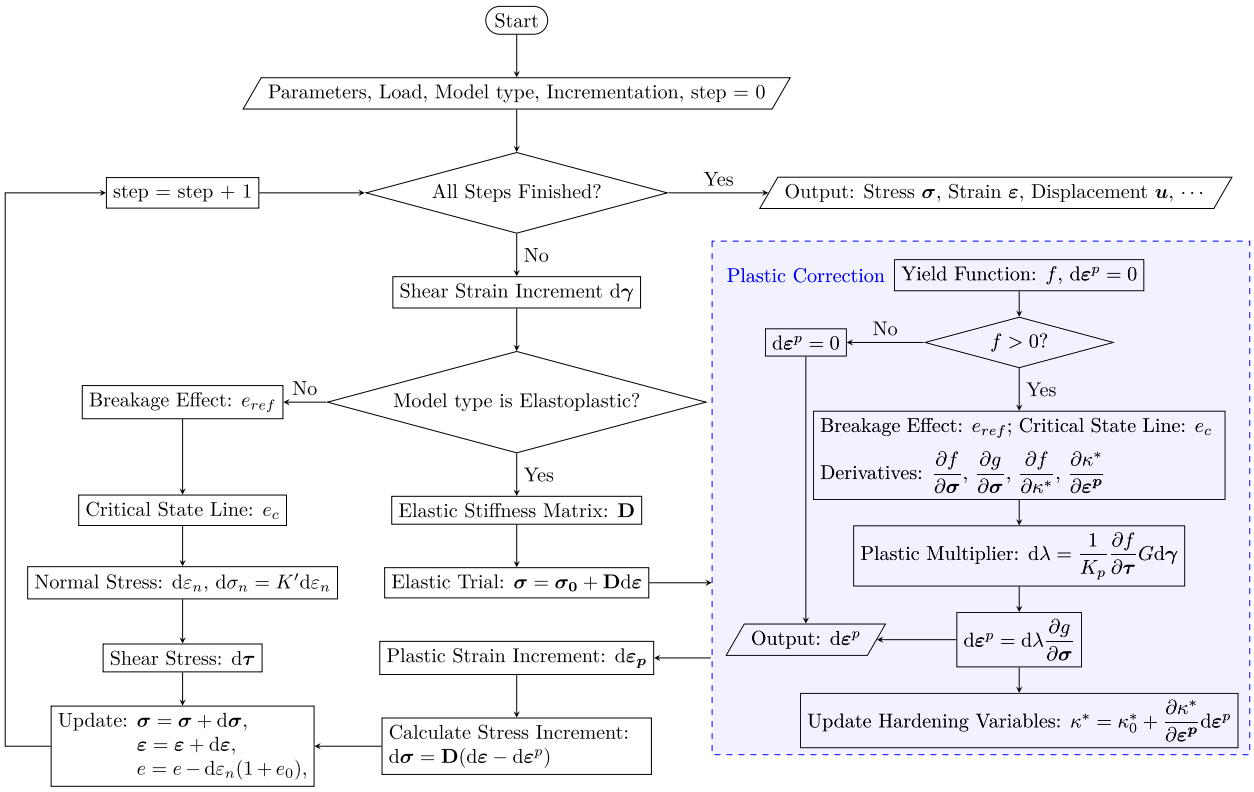

Fig. 2. Calculation procedure of the SSI models.

$$df(\boldsymbol{\sigma}, \kappa^*) = -\frac{\partial f}{\partial \sigma_n} \frac{K_n K'}{K_n + K'} d\lambda \frac{\partial g}{\partial \sigma_n} + \frac{\partial f}{\partial \boldsymbol{\tau}} G \left(d\boldsymbol{\gamma} - d\lambda \frac{\partial g}{\partial \tau} \right) + \sum \kappa^* \frac{\partial f}{\partial \kappa^*} \frac{\partial \kappa^*}{\partial \boldsymbol{\varepsilon}^p} d\lambda \frac{\partial g}{\partial \boldsymbol{\sigma}} = 0 \tag{5}$$

The plastic multiplier $d\lambda$ can be solved as

$$d\lambda = \frac{\frac{\partial f}{\partial \boldsymbol{\tau}} G d\boldsymbol{\gamma}}{\frac{K_n K'}{K_n + K'} \frac{\partial f}{\partial \sigma_n} \frac{\partial g}{\partial \sigma_n} + \frac{\partial f}{\partial \boldsymbol{\tau}} G \frac{\partial g}{\partial \boldsymbol{\tau}} - \sum \kappa^* \frac{\partial f}{\partial \kappa^*} \frac{\partial \kappa^*}{\partial \boldsymbol{\varepsilon}^p} \frac{\partial g}{\partial \boldsymbol{\sigma}}} = \frac{1}{K_p} \frac{\partial f}{\partial \boldsymbol{\tau}} G d\boldsymbol{\gamma} \tag{6}$$

Fig. 2 shows the calculation procedure of the SSI models. Cell "Model type is Elastoplastic?" directs the calculation to nonlinear incremental models if the answer is No. For all models, the explicit algorithm is used.

Development of SSI Models

In this section, six SSI models in total are introduced based on the previous framework. The SSI models are divided into two categories: three nonlinear incremental models (exponential, hyperbolic, and hypoplastic), and elastoplastic models (MCC, SANISAND, and SIMSAND). The exponential model was adopted from the existing soil–structure interface model; the hyperbolic model is proposed by changing the basic equation to a hyperbolic function in the exponential model (Clough and Duncan 1971); the hypoplastic, MCC, SANISAND, and SIMSAND models were converted directly from existing soil models.

Herein, variables in vectors are written in bold whereas normal symbols represent scalar variables or the norm of the vector. For example, $\boldsymbol{\tau}$ represents a vector of the shear stress with two elements representing the shear stress in two directions, whereas τ represents the norm of $\boldsymbol{\tau}$, i.e., $\tau = \|\boldsymbol{\tau}\| = \sqrt{\tau_s^2 + \tau_t^2}$.

Considerations of Some Important Features

Nonlinear Shear Modulus

To introduce the dependency of the stiffness on the soil densities and the stress levels, the equation of the nonlinear shear modulus G suggested by Richart et al. (1970) has been adopted

$$G = G_0 \frac{(2.97 - e)^2}{1 + e} \left(\frac{\sigma_n}{P_{at}} \right)^{n_g} \tag{7}$$

where n_g is an exponent that usually takes the value of 0.6; and G is used to calculate the current elastic shear modulus in the elastoplastic SSI models.

Critical State Concept

In this study, the following equation of the critical state line (CSL) proposed by Yin et al. (2018) is used except in the MCC-based model:

$$e_c = e_{\text{ref}} \exp \left[-\lambda \left(\frac{\sigma_n}{p_{at}} \right)^{\xi} \right] \tag{8}$$

where λ and ξ are two constants controlling the shape of the critical state line; p_{at} = standard atmospheric pressure; and e_{ref} = reference critical void ratio corresponding to the critical void ratio when the normal stress is zero. According to Yin et al. (2016), the density state effect on the stress–displacement strength behavior was implemented into the model using the following equations:

$$\tan \phi_p = \left(\frac{e_c}{e} \right)^{n_p} \tan \phi_c, \qquad \tan \phi_{pt} = \left(\frac{e}{e_c} \right)^{n_d} \tan \phi_c \tag{9}$$

where n_p and n_d are constants that control the degree of density effect in mobilized strength and stress dilatancy; and ϕ_c = critical

J. Geotech. Geoenviron. Eng., 2024, 150(7): 04024050

friction angle. The void ratio e is updated using the following equation:

$$\mathrm{d}e = -\mathrm{d}\varepsilon_n(1+e_0) \tag{10}$$

Particle Breakage Effect

To consider the effect of particle breakage, the modified energy-based formulation by moving downward in the $e-\ln\sigma_n$ space is adopted (Jin et al. 2018)

$$e_{\mathrm{ref}} = e_{\mathrm{ref}u} + (e_{\mathrm{ref}0} - e_{\mathrm{ref}u})\exp\left(-\rho\frac{w^{n_w}}{b+w^{n_w}}\right),$$
$$w = \int(\langle\sigma_n \mathrm{d}\varepsilon_n\rangle + \tau\mathrm{d}\gamma) \tag{11}$$

where $e_{\mathrm{ref}0}$ and $e_{\mathrm{ref}u}$ = initial and ultimate reference critical void ratio, respectively; ρ is a constant that controls the decreasing rate of the critical state line; $\langle\cdot\rangle$ is Macaulay brackets; and b, and n_w are model parameters that control the effect of the energy on particle breakage.

Exponential Model

The exponential model was adopted directly from Yang and Yin (2021). It uses the exponential shear stress–strain relation

$$\tau = \tan\phi_p\sigma_n[1-\exp(-a\gamma)] \tag{12}$$

The normal strain is controlled by stress–dilatancy behavior. In this model, a stress–dilatancy relation of Roscoe and Burland (1968) by modified Yin and Chang (2013) was adopted

$$\frac{\mathrm{d}\varepsilon_n^{\mathrm{in}}}{\mathrm{d}\gamma} = A_d(\tan\phi_{pt}-\eta) \tag{13}$$

where $\mathrm{d}\varepsilon_n^{\mathrm{in}}$ = induced normal strain that is similar to the induced elastoplastic normal strain. The normal stress–strain relation can be given by the following equation, similar to the elastoplastic models:

$$\mathrm{d}\sigma_n = K_n(\mathrm{d}\varepsilon_n - \mathrm{d}\varepsilon_n^{\mathrm{in}}) \tag{14}$$

Differentiating Eq. (12) and combining it with Eqs. (2), (13), and (14) obtains

$$\frac{\mathrm{d}\tau}{\mathrm{d}\gamma} = G(1-\eta/\tan\phi_p) + \frac{K_nK'}{K_n+K'}A_d(\tan\phi_{pt}-\eta) \times[\eta - a\gamma(\tan\phi_p-\eta)] \tag{15}$$

$$\frac{\mathrm{d}\varepsilon_n}{\mathrm{d}\gamma} = \frac{K_n}{K_n+K'}A_d(\tan\phi_{pt}-\eta) \tag{16}$$

Detailed descriptions of the model and the corresponding parameters were presented by Yang and Yin (2021).

Hyperbolic Model

The hyperbolic model is proposed by changing the basic equation in the exponential model to a hyperbolic function (Clough and Duncan 1971):

$$\tau = \tan\phi_p\sigma_n[\gamma/(a+\gamma)] \tag{17}$$

Similar to the exponential model, the incremental shear stress can be derived by differentiating Eq. (17)

$$\frac{\mathrm{d}\tau}{\mathrm{d}\gamma} = G(1-\eta/\tan\phi_p)[a/(a+\gamma)] + \frac{K_nK'}{K_n+K'}A_d(\tan\phi_{pt}-\eta) \times[\eta - a\eta/(a+\gamma)] \tag{18}$$

Other equations are exactly the same as in the exponential model.

Hypoplastic Model

Arnold and Herle (2006) and Stutz et al. (2017) proposed several hypoplastic interface models by introducing additional coefficients in the basic hypoplastic equation. Similar to the hypoplastic model, and to be consistent with the previously introduced dynamic peak friction angle and dynamic phase-transformation friction angle, a simple hypoplastic interface model is proposed. The following coefficients are introduced in the basic hypoplastic equation (Wang et al. 2018):

$$\mathrm{d}\boldsymbol{\sigma} = I_{se}\left[c_1\sigma_n\mathrm{d}\boldsymbol{\varepsilon} + c_2\mathrm{d}\varepsilon_n\boldsymbol{\sigma} + c_3\frac{\sum(\boldsymbol{\sigma}\mathrm{d}\boldsymbol{\varepsilon})}{\sigma_n}\boldsymbol{\sigma} + c_4(\boldsymbol{\sigma}+\boldsymbol{s})\|\mathrm{d}\boldsymbol{\varepsilon}\|I_e\right] \tag{19}$$

where $\boldsymbol{s} = [0,\tau_s,\tau_t]^T$ is the shear stress vector; $I_{se} = (e_c/e)^{n_p}$ (similar to $\tan\phi_p$) and $I_e = (e/e_c)^{n_d}$ (similar to $\tan\phi_{pt}$) are the critical state function and stiffness function, respectively; and c_1, c_2, c_3, and c_4 are constants that can be determined by simple CNL and CV experiments

$$\begin{aligned}&\mathrm{CV}:\mathrm{d}\tau_s|_{\gamma_s=0} = G\mathrm{d}\gamma_s, \mathrm{d}\tau_s|_{\gamma_s\to\infty} = 0\\ &\mathrm{CNL}:\mathrm{d}\sigma_n|_{\gamma_s=0} = 0, \mathrm{d}\sigma_n|_{\gamma_s\to\infty} = 0\\ &\Rightarrow\begin{cases} c_1 = \dfrac{G}{\sigma_{n0}I_{se0}}, c_2 = c_1\left[\dfrac{\sqrt{1+\nu_i^2}I_{e0}}{\mu\nu_i} - \left(1+\dfrac{1}{\mu^2}\right)\right]\\ c_3 = c_1/\mu^2, c_4 = -c_1/\mu\end{cases}\end{aligned} \tag{20}$$

where $\mu = \tan\phi_c = \tau_s/\sigma_n|_{\gamma_s\to\infty}$; and $\nu_i = \mathrm{d}\varepsilon_n/\mathrm{d}\gamma_s|_{\gamma_s=0}$. The incremental normal strain can be solved by combining Eq. (2) and the first component of Eq. (19)

$$\begin{aligned}&\mathrm{d}\varepsilon_n = -\frac{d_1d_2 + d_3\sqrt{d_1^2+d_4d_2^2-d_4d_3^2}}{d_2^2-d_3^2},\\ &d_1 = c_3(\tau_s\mathrm{d}\gamma_s+\tau_t\mathrm{d}\gamma_t)I_{se}, d_2 = -K' + \sigma_n(c_1+c_2+c_3)I_{se}\\ &d_3 = c_4\sigma_nI_eI_{se}, d_4 = (\mathrm{d}\gamma_s)^2+(\mathrm{d}\gamma_t)^2\end{aligned} \tag{21}$$

Assuming that the normal strain $\mathrm{d}\varepsilon_n$ in $\|\mathrm{d}\boldsymbol{\varepsilon}\|$ can be ignored, the Eq. (21) can be simplified as

$$\mathrm{d}\varepsilon_n = \frac{K_n'}{K_n'+K'}A_d'(\tan\phi_{pt}-\eta)\mathrm{d}\gamma \tag{22}$$

where $K_n' = (c_1+c_2+c_3)\sigma_nI_{se}$; and $A_d' = \nu_i/(\mu\sqrt{1+\nu_i^2}I_{e0}I_{se})$ which is very similar to the normal stiffness of soil K_n and dilatancy parameter A_d. For the shear stress, Eq. (19) can be rewritten

$$\frac{\mathrm{d}\boldsymbol{\tau}}{\mathrm{d}\boldsymbol{\gamma}} = I_{se}\left[c_1\sigma_n + c_2\tau\boldsymbol{\nu} + c_3\boldsymbol{\nu}(\sigma_n+\boldsymbol{\eta\tau}) + 2c_4\boldsymbol{\tau\nu}\sqrt{1+1/\nu_s^2+1/\nu_t^2}I_e\right] \tag{23}$$

where $\boldsymbol{\nu} = \mathrm{d}\varepsilon_n/\mathrm{d}\boldsymbol{\gamma}$.

Extended MCC Model

The extended MCC model is proposed to simulate both sand and clay interfaces with the introduction of a general yield surface combined with the MCC yield surface (Roscoe and Burland 1968) and the yield surface for crushing surface of sand (Hardin 1985) with a nonassociated flow rule

$$f = \frac{1}{n}\left(\frac{\eta}{M_c - m\eta}\right)^{n+1}\sigma_n + \sigma_n - \sigma_{ci}(1+\xi),$$
$$g = \frac{1}{n}\left(\frac{\eta}{M_c}\right)^{n+1}\sigma_n + \sigma_n - \sigma_{ci}(1+\xi) \tag{24}$$

where m and n are constants; $M_c = \tan\phi_c$; σ_{ci} = size of bounding yield surface; and ξ = bounding ratio. The hardening rules of ξ and σ_{ci} are

$$\mathrm{d}\chi = -\xi_c\chi\sqrt{\mathrm{d}\varepsilon_i^p \mathrm{d}\varepsilon_i^p}, \qquad \mathrm{d}\sigma_{ci} = \sigma_{ci}\frac{1+e_0}{\lambda-\kappa}\mathrm{d}\varepsilon_n^p \tag{25}$$

By introducing the bounding surface concept, the plastic moduli become the plastic moduli of the bounding surface ($\overline{K_p}$), and the plastic moduli of the current yield surface can be calculated as

$$K_p = \{1 + h_p[(\lambda-\kappa)\ln(\mathrm{OCR})]^2\mathrm{OCR}^{|M-\eta|}\}\overline{K_p}$$
$$\mathrm{OCR} = \frac{\sigma_{ci}(1+\chi)}{\sigma_{cd}}, \quad \sigma_{\mathrm{cd}} = \frac{1}{n}\left(\frac{\eta}{M_c - m\eta}\right)^{n+1}\sigma_n + \sigma_n \tag{26}$$

where OCR = overconsolidation ratio. The critical state line of the extended MCC model is represented by

$$e_c = e_{\mathrm{ref}} - \lambda\log\sigma_n \tag{27}$$

where λ is a model parameter.

SANISAND Model

The SANISAND interface model directly adopts the SANISAND soil model (Taiebat and Dafalias 2008) with no significant changes, which is similar to the SANISAND interface model proposed by Staubach et al. (2022a). It uses a wedge-like shape of yield surface

$$f = (\tau - \sigma_n\alpha)^2 - m^2\sigma_n^2\left[1 - \left(\frac{\sigma_n}{p_0}\right)^n\right] \tag{28}$$

where m and n are constants; α = rotation index; p_0 = yield stress in compression; and the term $[1-(\sigma_n/p_0)^n]$ is ignored in this study to be consistent with other models. The flow rule is represented by

$$\mathrm{d}\sigma_n = \mathrm{d}\lambda(Dr_{ef} + e^{-Vr_{ef}}), \qquad \mathrm{d}\tau = \mathrm{d}\lambda(sr_{ef} + X\eta e^{-Vr_{ef}}) \tag{29}$$

where X and V are model parameters; $r_{ef} = |\eta - \alpha|$; $D = sA_d(\alpha^d - \alpha)$; $s = (\tau - \sigma_n\alpha)/|\tau - \sigma_n\alpha|$; and α and α^d = rotation index and the rotation index associated with the dilatancy surface, respectively. Parameter V usually is a very large positive parameter, and the term $e^{-Vr_{ef}}$ is regarded as a transition mechanism caused by the change of the stress ratio. The hardening rule of α is

$$\mathrm{d}\alpha = \mathrm{d}\lambda h(\eta - \alpha)(\alpha^b - \alpha) \tag{30}$$

where α^b = rotation index associated with the bounding surface; and

$$h = \frac{b_0}{(b_{\mathrm{ref}} - s(\alpha^b - \alpha))^2}, \qquad b_0 = G_0 h_0(1 - c_h e)\left(\frac{p_{\mathrm{at}}}{\sigma_n}\right)^{1/2} \tag{31}$$

where h_0 and c_h are model parameters; $b_{\mathrm{ref}} = \alpha_c^b + \alpha_e^b$; and subscripts c and e represent compression and extension respectively. When $s = 1$, $\alpha^b = \alpha_c^b$ and $b_{\mathrm{ref}} - s(\alpha^b - \alpha) = (\alpha_e^b + \alpha)$, whereas for $s = -1$, $\alpha^b = -\alpha_e^b$ and $b_{\mathrm{ref}} - s(\alpha^b - \alpha) = (\alpha_c^b - \alpha)$. Detailed information was presented by Taiebat and Dafalias (2008).

SIMSAND Model

The SIMSAND interface model directly adopted the SIMSAND soil model (Yin et al. 2016), with no significant changes. It uses a nonlinear form of the Mohr–Coulomb model's yield surface

$$f = \eta - \frac{\tan\phi_p\gamma^p}{k_p + \gamma^p} \tag{32}$$

where k_p is a constant; and γ^p = total plastic shear strain. The flow rule of the SIMSAND SSI model is represented by

$$\mathrm{d}\sigma_n = A_d(\tan\phi_{pt} - \eta)\mathrm{d}\lambda, \qquad \mathrm{d}\tau = \eta\mathrm{d}\lambda, \qquad \frac{\mathrm{d}\gamma^p}{\mathrm{d}\boldsymbol{\varepsilon}^p} = \left[0, \frac{\gamma_s^p}{\gamma^p}, \frac{\gamma_t^p}{\gamma^p}\right] \tag{33}$$

For all six SSI models, the nonlinear shear modulus, critical state concept, and particle breakage effect are all considered, except that the linear critical state line in $e - \log\sigma_n$ space represented by Eq. (27) is adopted and the breakage effect is not adopted in the MCC SSI model.

Summary of Model Parameters

Table 1 presents the required parameters for the SSI models.

The surface roughness of the soil–structure interface is not considered explicitly in these models. Research has shown that surface roughness plays a significant role in interface behaviors (Potyondy 1961; Uesugi and Kishida 1986; Stutz 2016). In this study, the effect of the roughness is considered using the frictional property ϕ_c of the interface. The degradation of the surface roughness and other surface characteristics such as the surface morphology are not considered in this study.

Evaluation of the Interface Models

This section uses different evaluation criteria to evaluate the performance of different models. To evaluate these models under various different conditions, a sand–steel interface with a large range of stress levels (initial normal stress of 60, 100, 120, and 310 kPa), different boundary conditions (CNL and CNS with stiffness of 1,000, 2,000, and 5,000 kN/mm), and different soil densities (dense and loose) were collected from Pra-Ai (2013). Table 2 presents the details of the experiments used in this study. The tests were conducted using a direct shear test apparatus in the 3SR laboratory (Sols, Solides, Structures - Risques, France) with different initial normal stress (60, 100, 120, and 310 kPa), different boundary conditions (CNL and CNS with the normal stiffness of 1,000, 2,000, and 5,000 kN/mm), and different soil densities (dense sand and loose sand) on Fontainebleau sand–steel interface.

To investigate the behaviors of the clay–structure interface experiments, a series of CNL tests on the kaolin clay–steel interface conducted by Martinez and Stutz (2019) also were collected for evaluation. The tests were conducted using the direct shear testing device with shearing rates of 0.02, 0.06, 0.2, 0.5, 1, 2, and

Table 1. Required parameters of SSI models

Category	Symbol	Description	Models
Thickness	d_{50}	Mean particle size	All models
	R_d	Ratio of thickness of sand layer to median grain size d_{50}	All models
Void ratio	e_0	Initial void ratio	All models
Elastic stiffness	G_0	Reference shear modulus	All models
	n_g	Exponent in equation of nonlinear shear modulus; usually 0.6	All models
	R	Ratio of elastic normal modulus to elastic shear modulus	Except hypoplastic
CSL	ϕ_c	Critical friction angle	All models
	$e_{\text{ref}0}$	Initial reference critical void ratio	All except MCC
	λ	Slope of critical state line in $e - \ln \sigma_n$ space	All models
	κ	Slope of swelling line	MCC
	ξ	Constant that controls shape of critical state line	All except MCC
	n_p, n_d	Constants that control effect of density of soil on hardening and softening behaviors of interface	All except MCC
Dilatancy	A_d	Constant that controls effect of dilatancy	All except hypoplastic
	ν_i	Initial dilatancy slope	Hypoplastic
Breakage	$e_{\text{ref}u}$	Ultimate reference critical void ratio due to particle breakage	All except MCC
	ρ	Constant that controls decreasing rate of critical state line due to particle breakage	All except MCC
	n_w b,	Constants that control effect of energy on breakage index	All except MCC
Yield surface	m, n	Constants that control shape of yield surface	MCC and SANISAND
	k_p	Constant that controls shape of yield surface	SIMSAND
	σ_{c0}	Initial size of yield surface	MCC
Hardening	χ_0, ξ_c	Initial bounding ratio and hardening parameter for bounding ratio	MCC
	h_p	Hardening parameter to control effect of overconsolidation	MCC
	h_0, c_h	Stress-ratio-related hardening parameters	SANISAND

Table 2. Properties of Fontainebleau sand–steel interface experiments

BC	D_{50} (mm)	$e_{\max}$	$e_{\min}$	e	D_r (%)	K (kN/mm)	σ_{n0} (kPa)
CNL	0.23	0.866	0.545	0.76, 0.57	30, 90	0	60, 120, 310
CNS	0.23	0.866	0.545	0.76, 0.57	30, 90	1,000, 2,000, 5,000	100, 310

Table 3. Properties of kaolin clay–steel interface experiments

Shear displacement rate (mm/min)	Normal stress (kPa)	OCR	Initial void ratio
0.02, 0.06, 0.2, 0.5, 1, 4	75	1	1.38, 1.37, 1.37, 1.37, 1.36, 1.39
0.02, 0.2, 0.5, 2	75	5	1.23, 1.23, 1.21, 1.24

Note: kaolin clay properties: aspect ratio = 28:1; $L_L = 59.8\%$; $C_c = 0.31$; $C_s = 0.14$; 52% of particles by mass are smaller than 2 μm; for normal consolidated specimens $c_v = 0.007$ cm^2/s.

4 mm/min on the kaolin clay–steel interface. Table 3 presents detailed information for the experiments.

Optimization-Based Identification of Model Parameters

Model calibration is a common method to obtain the best fit of the parameters according to the experiment data. To eliminate manual errors, optimization-based inverse analysis was adopted herein for all models. Assuming that $\mathbf{Y}^{\text{obs}}_{\tau|\sigma_n|u_n}$ represents the observed experimental data, $\mathbf{Y}^{\text{pre}}_{\tau|\sigma_n|u_n}(\mathbf{X})$ represents the predicted data by the analytical model, where $\mathbf{X}$ is the model parameters. Model calibration is the process to minimize the difference between the observed data and the predicted data

$$\mathbf{X} = \arg\min_{\mathbf{X}} \{\text{dist}[\mathbf{Y}^{\text{obs}}_{\tau|\sigma_n|u_n}, \mathbf{Y}^{\text{pre}}_{\tau|\sigma_n|u_n}(\mathbf{X})]\} \tag{34}$$

where $\text{dist}(\cdot)$ is a function that describes the distance between $\mathbf{Y}^{\text{obs}}_{\tau|\sigma_n|u_n}$ and $\mathbf{Y}^{\text{pre}}_{\tau|\sigma_n|u_n}(\mathbf{X})$, and usually is defined as the RMS error (RMSE) of the relative difference

$$\text{dist}[\mathbf{Y}^{\text{obs}}_{\tau|\sigma_n|u_n}, \mathbf{Y}^{\text{pre}}_{\tau|\sigma_n|u_n}(\mathbf{X})] = \sum_i l_i \left\| \frac{\mathbf{Y}^{\text{pre}}_i(\mathbf{X}) - \mathbf{Y}^{\text{obs}}_i}{\text{T}(\mathbf{Y}^{\text{obs}}_i)} \right\|, \quad i \in \{\tau, \sigma_n, u_n\} \tag{35}$$

where $\|\cdot\|$ represents the norm operator; $\text{T}(\mathbf{Y}^{\text{obs}}_{\tau|\sigma_n|u_n})$ represents the range of observations; and l_i = corresponding weights. To solve Eq. (34), an optimization method is required to minimize Eq. (35). The covariance matrix adaption evolution strategy (CMA-ES) algorithm (Hansen 2023) with the default optimization parameters described by Hansen (2016) and Hansen et al. (2019) was used in the calibration.

Based on the optimization-based parameter identification, model parameters for Fontainebleau sand–steel interface experiments and the kaolin clay–steel interface experiments are listed in Tables 4 and 5, respectively. The particle breakage effect was not considered in modeling the kaolin clay–steel interface experiments because it is

J. Geotech. Geoenviron. Eng., 2024, 150(7): 04024050

Table 4. Calibrated model parameters for Fontainebleau sand–steel interface experiments

	Model					
Parameter	Exponential	Hyperbolic	Hypoplastic	MCC	SANISAND	SIMSAND
R_d	6.3	5.3	6.5	10.5	6.1	6.3
ϕ	30.9	30.6	31	32.1	31.3	31.9
e_{refu}	0.65	0.67	0.06	—	0.67	0.61
b	379	800	1,623	—	2022	298
ρ	28.1	1.5	242.6	—	235.5	57.9
n_w	0.48	1.55	0.14	—	0.47	0.33
λ	0.023	0.024	0.013	0.031	0.022	0.014
κ	—	—	—	0.003	—	—
ξ	0.963	0.999	1	—	0.984	0.984
e_{ref0}	0.79	0.78	0.93	—	0.82	0.87
n_p	1.15	1.86	2.52	—	1.17	3.04
n_d	0.57	0.8	0.83	—	0	0
A_d	0.93	0.69	—	—	1.09	0.93
G_0	275.6	376.5	435.6	412.3	358	327.4
R	4.76	9.97	—	3.26	5.8	6.06
v_i	—	—	0.73	—	—	—
ξ_c	—	—	—	8.9	—	—
χ_0	—	—	—	84	—	—
h_p	—	—	—	1,431.50	—	—
n	—	—	—	1	20	—
m	—	—	—	0.65	0.05	—
h_0	—	—	—	—	0.1	—
c_h	—	—	—	—	1	—
k_p	—	—	—	—	—	0.063
Fitness (%)	14.70	14.40	13.80	15.60	14.30	15.00

Table 5. Calibrated model parameters for kaolin clay–steel interface experiments

	Model					
Parameter	Exponential	Hyperbolic	Hypoplastic	MCC	SANISAND	SIMSAND
d_s	1.57	2.5	2.85	1.17	1.17	2.41
ϕ	31.5	28.3	28.7	31.3	26.1	26.2
λ	4.126	2.897	2.982	0.487	0.284	1.04
κ	—	—	—	0.03	—	—
ξ	0.952	0.821	0.249	—	1.727	1.235
e_{ref0}	4.86	6.13	13.7	—	0.1	1.13
n_p	0.55	0.4	0.01	—	0	0
n_d	1	0.01	0.91	—	0.01	0.33
A_d	0.05	0.5	—	—	0.76	0.07
G_0	174.9	188.5	300.1	308.2	160	219.6
R	4.23	2.83	—	0.68	0.62	0.08
v_i	—	—	9.94	—	—	—
ξ_c	—	—	—	65.2	—	—
χ_0	—	—	—	850	—	—
h_p	—	—	—	73,905.1	—	—
n	—	—	—	0.36	20	—
m	—	—	—	0.69	0.05	—
h_0	—	—	—	—	0.1	—
c_h	—	—	—	—	0.1	—
k_p	—	—	—	—	—	0.27
Fitness (%)	12.10	11.80	11.80	9.90	11.70	13.20

proposed only for sand. All model parameters were fitted to the experiments, and they were restricted by their physical meanings. The same model parameters may not be the same for different models even though they have the same meanings. Figs. 3–10 show the data from the simulations and experiments under different conditions. All models generally were able to simulate the interface behaviors under different conditions.

To ensure that the models were not overfitted, *k*-folds cross-validation (Kohavi 1995) was employed for evaluating their performance. The experiments were divided randomly into five folds; four folds were allocated for calibration, and the remaining fold was used for validation. This process was repeated five times, and the average fitness was utilized to assess the performance of the models. Fig. 11 shows the results of the *k*-folds cross-validation. In Fig. 11, lines represent the calibration accuracy, and arrows represent the validation accuracy. The results indicate that when the calibration folds are randomly selected, the accuracy of the validation fold consistently remains at an acceptable level.

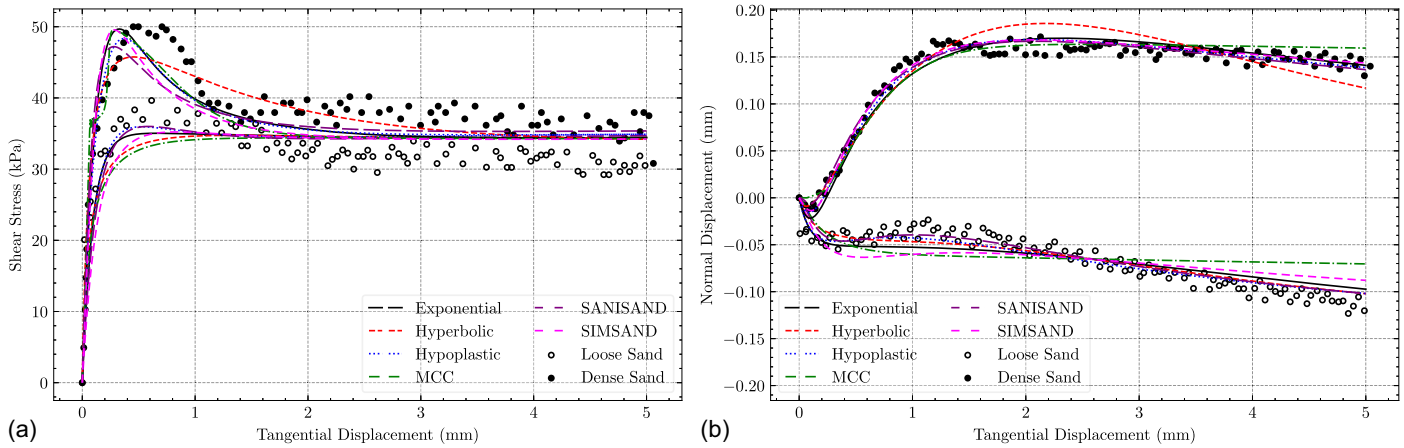

Fig. 3. Simulation results of Fountainbleau sand–steel CNL experiments with the normal stress of 60 kPa: (a) shear stress; and (b) normal displacement.

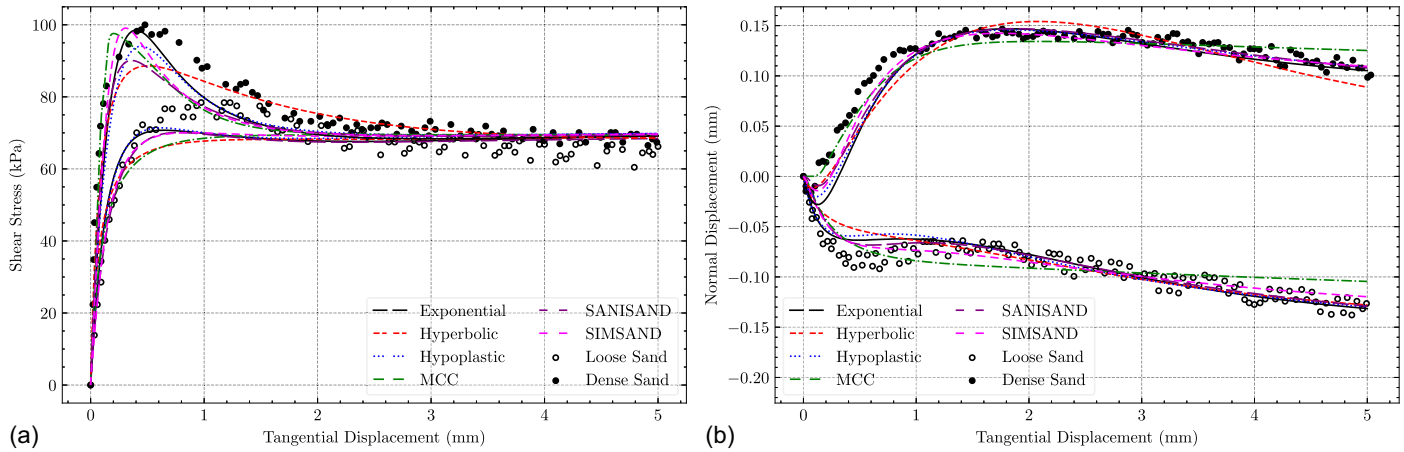

Fig. 4. Simulation results of Fountainbleau sand–steel CNL experiments with the normal stress of 120 kPa: (a) shear stress; and (b) normal displacement.

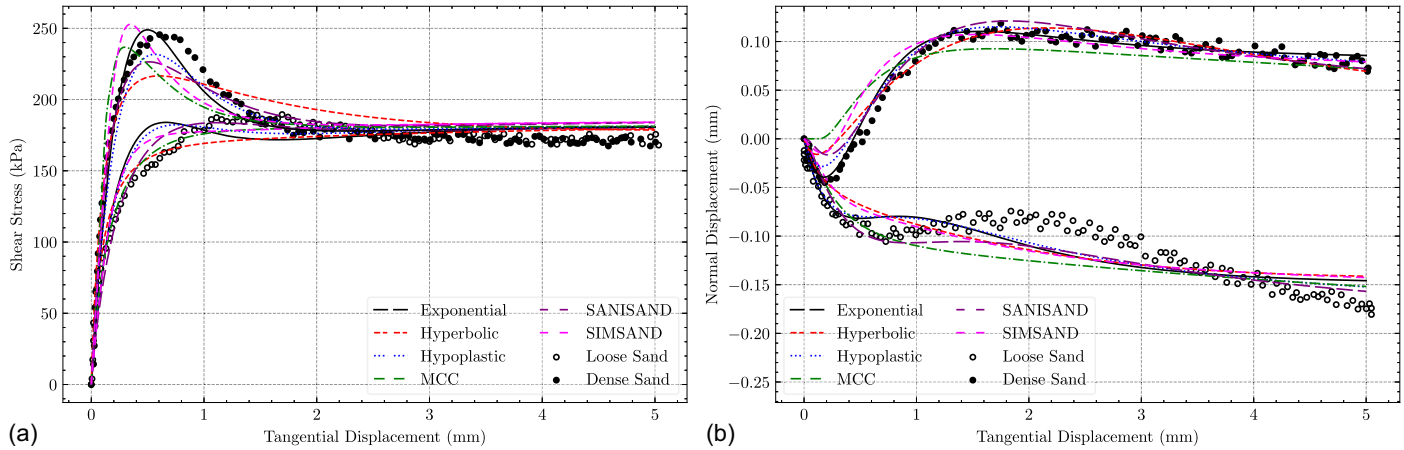

Fig. 5. Simulation results of Fountainbleau sand–steel CNL experiments with the normal stress of 310 kPa: (a) shear stress; and (b) normal displacement.

J. Geotech. Geoenviron. Eng., 2024, 150(7): 04024050

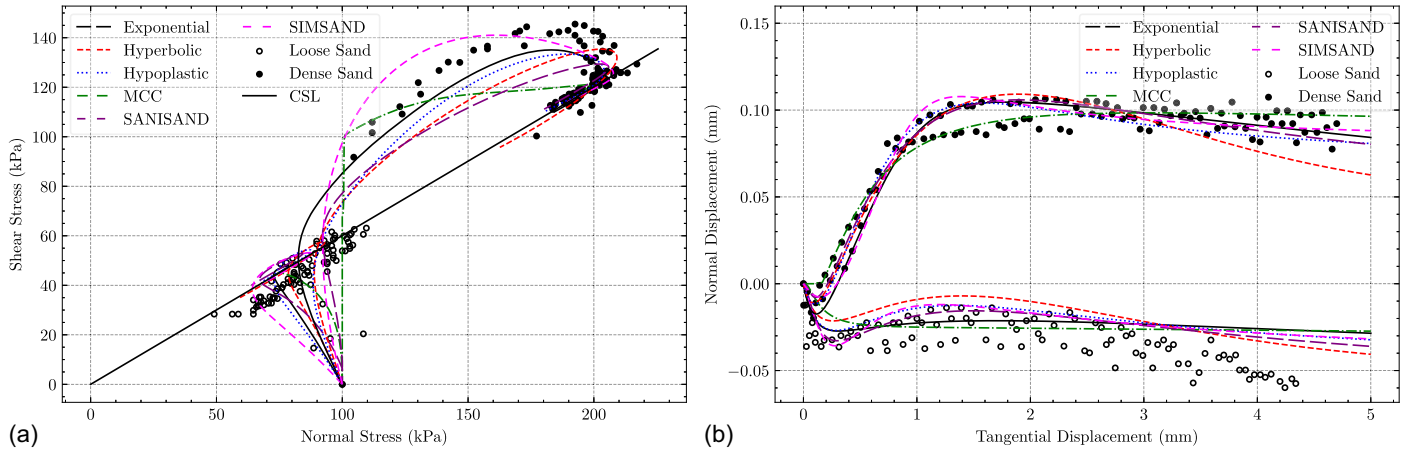

Fig. 6. Simulation results of Fountainbleau sand-steel CNS experiment with the normal stress of 100 kPa and normal stiffness of 1,000 kN/mm: (a) shear stress–normal stress curve; and (b) normal displacement–tangential displacement curve.

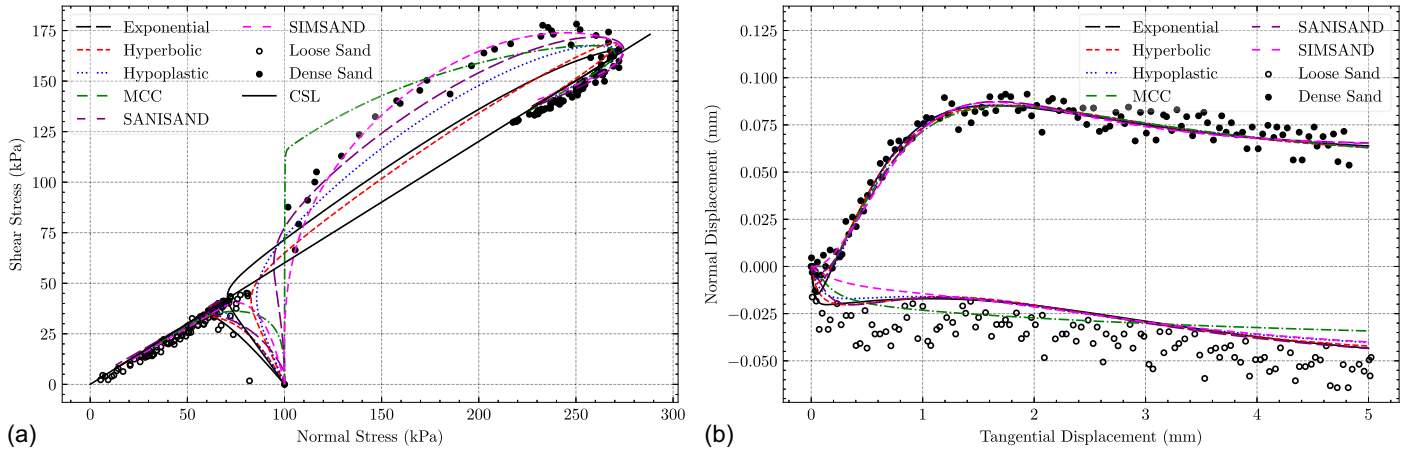

Fig. 7. Simulation results of Fountainbleau sand-steel CNS experiment with the normal stress of 100 kPa and normal stiffness of 2,000 kN/mm: (a) shear stress–normal stress curve; and (b) normal displacement–tangential displacement curve.

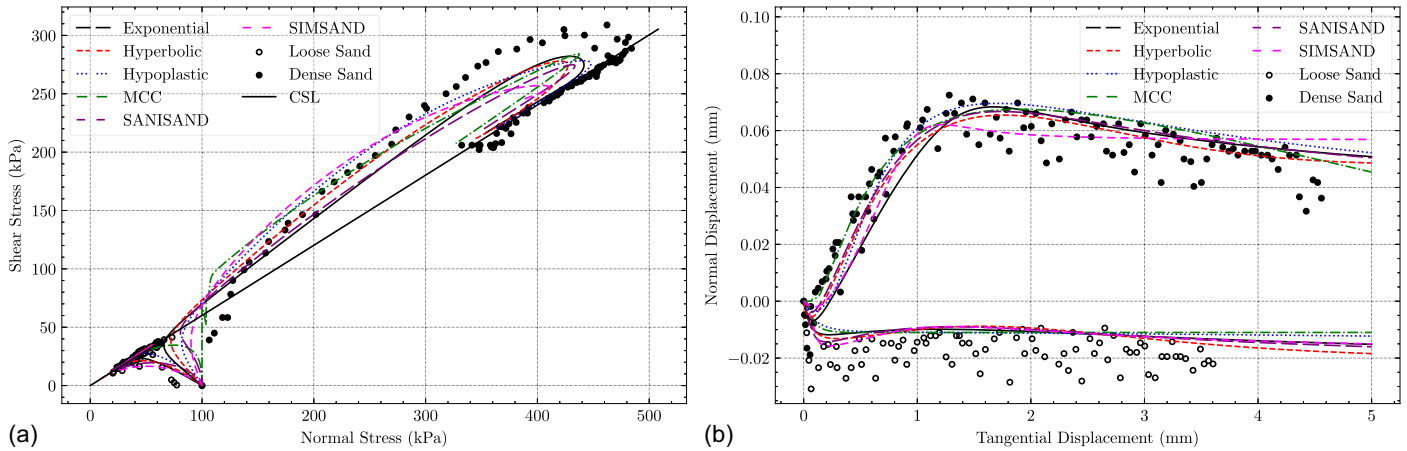

Fig. 8. Simulation results of Fountainbleau sand-steel CNS experiment with the normal stress of 100 kPa and normal stiffness of 5,000 kN/mm: (a) shear stress–normal stress curve; and (b) normal displacement–tangential displacement curve.

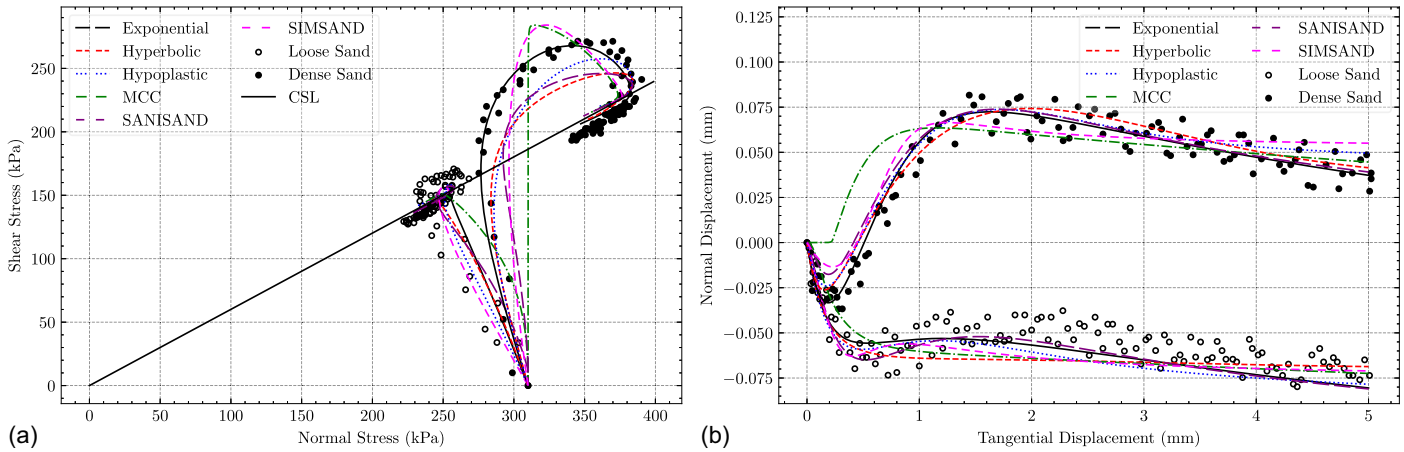

Fig. 9. Simulation results of Fountainbleau sand-steel CNS experiment with the normal stress of 310 kPa and normal stiffness of 1,000 kN/mm: (a) shear stress–normal stress curve; and (b) normal displacement–tangential displacement curve.

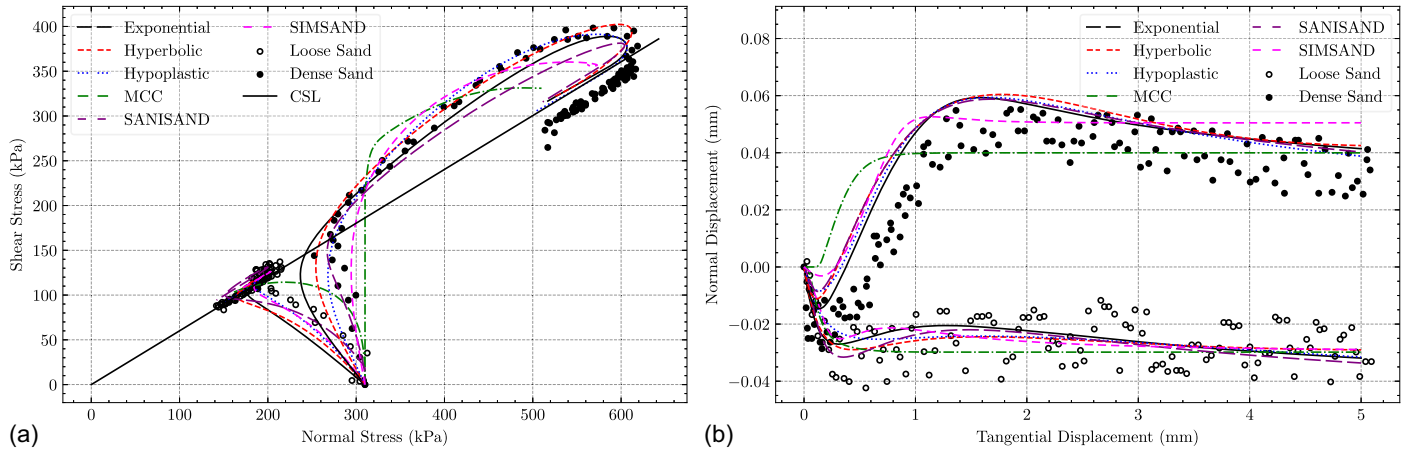

Fig. 10. Simulation results of Fountainbleau sand-steel CNS experiment with the normal stress of 310 kPa and normal stiffness of 5,000 kN/mm: (a) shear stress–normal stress curve; and (b) normal displacement–tangential displacement curve.

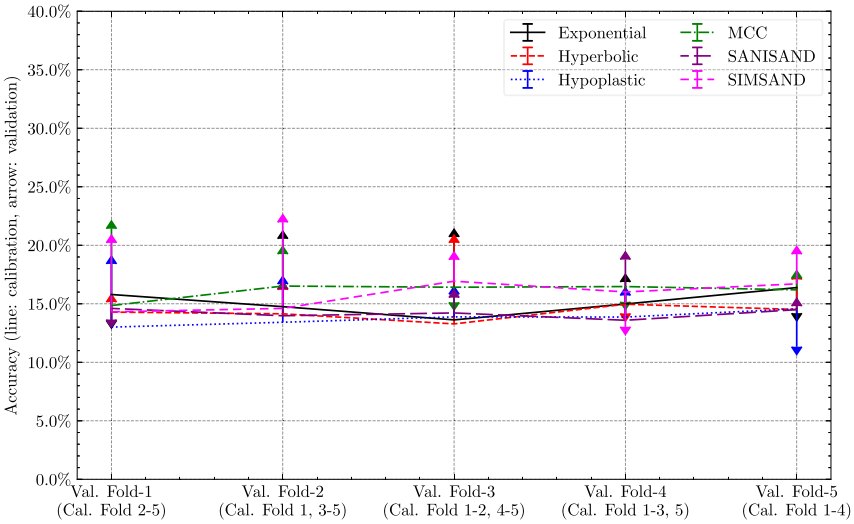

Fig. 11. Results of k-folds cross-validation. Val. = validation; and Cal. = calibration.

Table 6. Objective fitness function and coefficient of determination for different models and experiments

Goodness	Experiment	Exponential	Hyperbolic	Hypoplastic	MCC	SANISAND	SIMSAND
Fitness (%)	All	14.7	14.4	13.8	15.6	14.3	15.0
	CNL	7.1	7.7	6.7	9.0	6.5	8.0
	CNS, 100 kPa	11.8	11.9	12.6	17.4	11.2	11.5
	CNS, 310 kPa	9.0	9.9	9.6	12.0	9.8	13.2
R^2	All	0.28	0.27	0.36	0.30	0.29	0.21
	CNL	0.84	0.83	0.85	0.75	0.86	0.79
	CNS, 100 kPa	0.53	0.54	0.44	0.17	0.58	0.50
	CNS, 310 kPa	0.80	0.77	0.77	0.64	0.77	0.61

Moreover, the impact of various calibration folds on the accuracy of the validation fold was relatively minor; the greatest difference was less than 10%.

Global Comparisons Based on Information Criterion

With the identification of the model parameters, global assessments can be made to select the most suitable model for modeling the interface behaviors. A model information criterion (MIC) can be used to evaluate the performance of the models considering the goodness of fit and model complexity. The most commonly used MIC is the Akaike information criterion (AIC) (Akaike 1974), Knabe et al. (2012) simplified the AIC for the case of minimizing the sum of squared errors assuming that the residuals are independent and normally distributed

$$\text{AIC} = 2k - 2\ln(L) \approx 2k + n\ln s^2 \approx 2k + n\ln\left(\frac{1-R^2}{n}\right) \quad (36)$$

where k = number of model parameters; L = maximum likelihood value; n = number of data points; and s^2 = residual error variance. AICc (Hurvich and Tsai 1989) and the Bayesian information criterion (BIC) (Schwarz 1978) are two other MICs commonly used for cases in which there are insufficient data points

$$\text{AICc} = \text{AIC} + \frac{2k(k+1)}{n-k-1}, \qquad \text{BIC} = k\ln n - 2\ln(L) \quad (37)$$

Table 6 presents the objective function values and coefficient of determination for different models and experiments. The accuracy of the predictions of the different models was very close, the overall objective function values varied from 14.3% to 15.6%. The hypoplastic model had the best performance in terms of the prediction accuracy, followed by the SANISAND model, hyperbolic model, exponential model, SIMSAND model, and MCC model. The MCC model had the worst performance because it does not adopt a complex nonlinear critical state line and the particle breakage effect.

Table 7 presents the preferred models for different experiments based on different criteria. Because the number of model parameters was relatively close in the different models (14, 14, 13, 10, 17, and 15 parameters), the model selection largely is dependent on the goodness of fit. Overall, the hypoplastic, exponential, and SANISAND models performed better than the other models. The hypoplastic model is preferred for CNL experiments, the SANISAND model is preferred for CNS experiments under low confining pressure, and the exponential model is preferred for CNS experiments under high confining pressure. The aforementioned results were derived solely from experiments conducted on the specific soil–structure interface experiments, and should be regarded only as a reference for selecting a suitable model. To determine the most suitable model in practice, it is essential to compare these results with those of other experiments.

Table 7. Model selection for different experiments

Experiment	AIC	AIC_c	AIC_{r^2}	BIC
All	Hypoplastic	Hypoplastic	Hypoplastic	Hypoplastic
CNL	Hypoplastic	Hypoplastic	SANISAND	Hypoplastic
CNS, 100 kPa	SANISAND	SANISAND	SANISAND	SANISAND
CNS, 310 kPa	Exponential	Exponential	Exponential	Exponential

In general, the nonlinear elastic models not only had better performance in predicting the experiments but also required less computational time, and all three models had similar performance in several aspects. Of the elastoplastic models, the SANISAND and SIMSAND models had predictive accuracy similar to that of the nonlinear models, but they required much more computational time than nonlinear elastic models. The MCC model had the worst performance in almost all aspects, but the computational time required was less than that of the other two elastoplastic models because of the simplicity of its constitutive equations compared with those of the SANISAND and SIMSAND models.

Effect of Soil Density on the Shear Stress

Extensive studies have shown that the density of the soil has a significant effect on the behavior of the soil–structure interface. Yasufuku et al. (2003), Taha and Fall (2013) showed that increased density indicates a higher number of contacts between soil particles, resulting in higher shear strength. DeJong et al. (2006), DeJong and Westgate (2009) demonstrated that the volumetric behavior of the interface is highly dependent on the relative density; dense sand dilates after the initial contraction, and loose sand contracts during the shearing. For dense sand, Taha and Fall (2013, O'Rourke et al. (1990) argued that higher density also leads to higher peak shear strength, which could be attributed to the higher interlocking forces.

Fig. 12 shows the effect of the density on the peak shear stress based on the constant normal load experiments with an initial normal stress of 310 kPa. It describes the relationship between the peak stress ratio $\eta_{\max} = \tau_{\max}/\sigma_n$ and relative density D_r or overconsolidation ratio (for the MCC model). Different relative densities D_r or overconsolidation ratios were generated with different initial void ratios e_0. For loose sand or clay with lower OCR, the peak stress ratio remains stable at a relatively low value. This is because the soil is consistently contracted during shearing, and therefore the stress ratio always is less than the critical stress ratio. When the relative density is greater than about 40%–50% or the OCR is

greater than about 10, the peak stress ratio increases rapidly with the increase of the relative density or OCR. In this case, the soil dilates after the initial contraction, leading to a higher number of contacts between soil particles and thus a higher peak stress ratio. The stress ratio increases slightly more than linearly compared with the relative density or OCR, which is consistent with the results of O'Rourke et al. (1990).

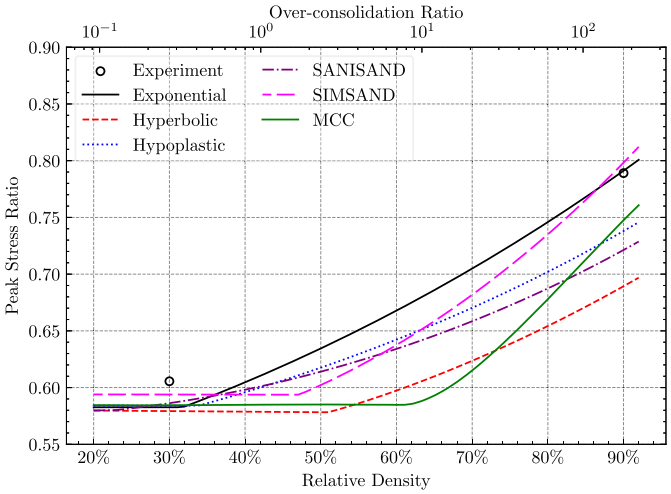

Fig. 12. Effect of the soil density on the peak shear stress.

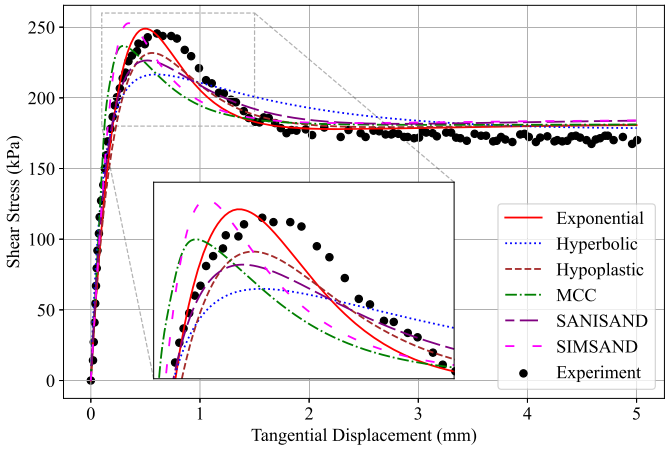

Fig. 13. Evolution of the shear stress.

Moreover, the exponential model and the SIMSAND model predicted the experimental results well, whereas other models underestimated the peak stress ratio for dense sand ($D_r = 90\%$). The influence of the relative density in the exponential model and the SIMSAND model was greater than that in the hyperbolic, hypoplastic, and SANISAND models (Fig. 13). Taking the exponential model and the hyperbolic model as an example, for the same initial shear modulus, the exponential model increases to stable stress faster than the hyperbolic model. For medium sand, the stress ratio of the exponential model is larger than that of the hyperbolic at the same shearing displacement. Thus, the density effect of the exponential model is more obvious than that of the hyperbolic model for dense sand. This also applies to the hypoplastic model, the SANISAND model, and the SIMSAND model. Therefore, the exponential model and the SIMSAND model are suitable for situations in which the density effect plays a very important role.

Effect of Interface Stiffness and Dilatancy Behavior

Figs. 14 and 15 show the peak and residual shear stress ratios and normal displacement under different boundary conditions with an initial normal stress of 100 kPa for Fountainbleau sand–steel interface experiments. The shear stress ratio increased with the increase of interface normal stiffness for dense sand, whereas the opposite was true for loose sand. The normal displacement decreased with the increase of the interface normal stiffness for dense sand, whereas the oppsite is true for loose sand. This was because the interface tends to dilate during shearing for dense sand. Because the interface's normal boundary is constrained by a spring with stiffness K, the normal stress increases, whereas the normal displacement decreases with the increase of the normal stiffness. Furthermore, all models except the MCC model were able to predict the shear stress and normal displacement satisfactorily. The MCC model predicted the shear stress well at small interface stiffness, and it predicted the normal displacement well at large interface stiffness. Moreover, the MCC model behaved differently when simulating experiments with dense sand and loose sand.

To explain this phenomenon, the evolution of the normal displacement for different models is as follows:

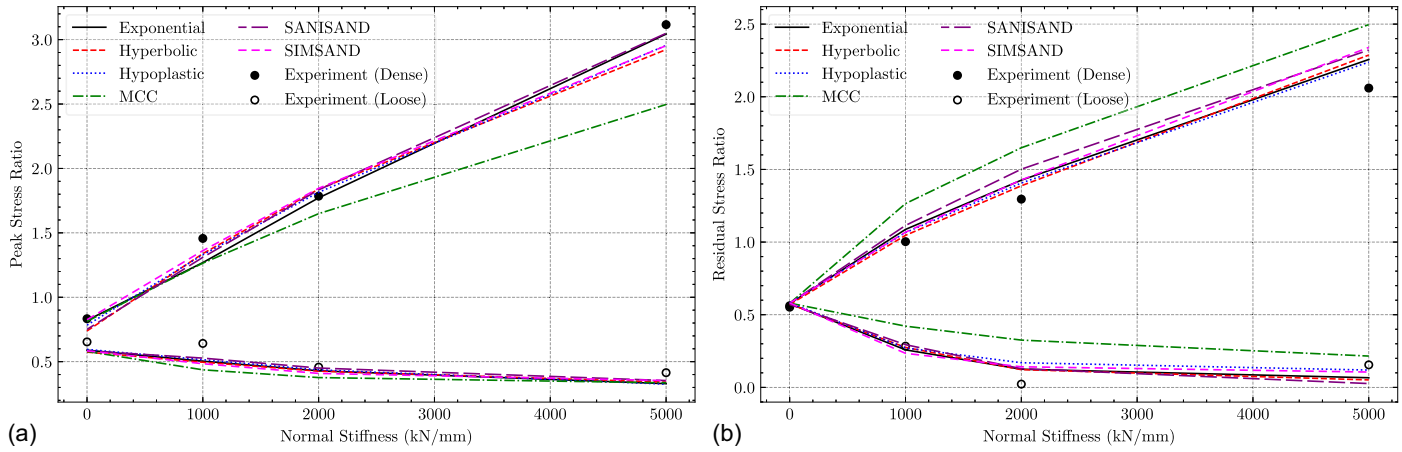

Fig. 14. Simulation results of the relative peak and residual shear stress ratio (shear stress/initial normal stress) under different boundary conditions: (a) peak stress ratio; and (b) residual stress ratio.

J. Geotech. Geoenviron. Eng., 2024, 150(7): 04024050

$$d\varepsilon_n = \frac{K_n^*}{K_n^* + K'} d\gamma^* \times \begin{cases} A_d^*(\tan\phi_{pt} - \eta) & \text{all except MCC and SANISAND} \\ A_d^*(\alpha^d - \alpha) & \text{SANISAND} \\ \dfrac{M_c^{n+1} - \eta^{n+1}}{(n+1)/n \cdot \eta^n} & \text{MCC} \end{cases} \tag{38}$$

where $K_n^* = K_n'$ and $A_d^* = A_d'$ for hypoplastic model, and $K_n^* = K_n$ and $A_d^* = A_d$ for other models; and $d\gamma^* = d\gamma$ for nonlinear elastic models and $d\gamma^* = d\gamma^p$ for elastoplastic models. Eq. (38) indicates that the normal behavior is controlled by both the interface's normal boundary condition (represented by the stiffness K') and the soil's normal behavior (represented by the soil's normal stiffness K_n and the dilatancy behavior). When the normal boundary of the interface is not constrained ($K' = 0$), Eq. (38) degenerates into stress–dilatancy equations similar to the general soil models. When the normal boundary of the interface is fixed ($K' = \infty$), the normal displacement is fixed to zero for both dense sand and loose sand. For the case of constant interface stiffness ($K' = \text{const}$), the stress and displacement states are intermediate between the two aforementioned cases. Because the stiffness item $K_n^*/(K_n^* + K')$ is the same for all models, the misprediction of the normal displacement for the MCC model is caused mainly by the dilatancy behavior. With the increase of the interface stiffness K', the effect of the dilatancy behavior on the normal displacement decreases, and thus the MCC model tends to simulate the normal displacement well at large interface stiffness. The following equation shows the evolution of the normal and shear stress:

$$d\sigma_n = -K' d\varepsilon_n \simeq \frac{K_n^* K'}{K_n^* + K'} d\gamma^* \begin{cases} A_d^*(M_{pt} - \eta) & \text{all except MCC} \\ \dfrac{M_c^{n+1} - \eta^{n+1}}{(n+1)/n \cdot \eta^n} & \text{MCC} \end{cases}, \quad \rho(d\tau, d\sigma_n) > 0 \tag{39}$$

where $\rho(d\tau, d\sigma_n) > 0$ indicates that the shear stress caused by the normal stress is positively correlated with the normal stress, which can be proved using Eqs. (6), (15), and (18), (23). Eq. (39) shows that unlike the normal displacement, the effect of the dilatancy behavior on the shear stress increases with the increase of the interface stiffness K', and thus the MCC model tends to simulate the shear stress well at small interface stiffness and to overestimate the shear stress at large interface stiffness.

The preceding analysis shows that the mispredictions of the shear stress and normal displacement are affected mainly by the dilatancy behavior in which the boundary condition increases and decreases the degree of the effect. Because the SANISAND model uses similar equation for the dilatancy surface α^d compared to $\tan\phi_{pt}$, and the rotation index α is very close to the stress ratio η, Eq. (38) can be generalized as

$$d\varepsilon_n \simeq \frac{K_n^*}{K_n^* + K'} d\gamma^* \begin{cases} A_d^*(M_{pt} - \eta) & \text{all except MCC} \\ \dfrac{M^{n+1} - \eta^{n+1}}{(n+1)/n \cdot \eta^n} & \text{MCC} \end{cases} \tag{40}$$

For all models except the MCC model, the phase transformation stress ratio M_{pt} is a function of the current density state and the critical state

$$M_{pt} = \left(\frac{e}{e_c}\right)^{n_d} M_c \tag{41}$$

where M_c = slope of critical state line. Eq. (41) for the dynamic phase transformation stress ratio M_{pt} implies that in loose sand with $e > e_c$, M_{pt} is greater than M_c, which leads to persistent shear contraction behaviors; in dense sand with $e < e_c$, M_{pt} is less than M_c, which allows the dense sand to be contracted and then dilated. For the MCC model, the phase transformation stress ratio M_{pt} equals the critical stress ratio M_c, which leads to the underestimation of the normal displacement for dense sand and overestimation of the normal displacement for loose sand compared with other models according to Eq. (40). This is consistent with the simulation results shown in Fig. 15. In contrast, the peak shear stress varies in the opposite direction, which can be explained similarly as the normal displacement. Similar to the normal displacement, it can be explained by the interlocking effect represented by the dynamic peak stress ratio M_p

$$M_p = \left(\frac{e_c}{e}\right)^{n_p} M_c \tag{42}$$

Based on the preceding analysis, because the MCC model does not consider density-dependent interlocking and the dilatancy effect, it cannot predict the normal and tangential behaviors correctly under various conditions. The model cannot be sued to predict

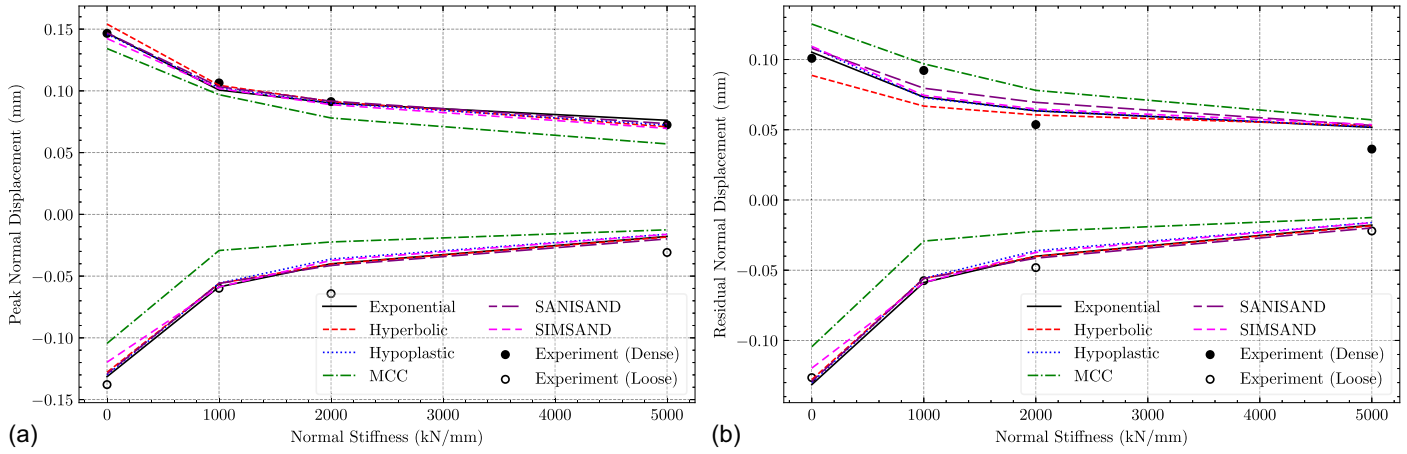

Fig. 15. Simulation results of the relative peak and residual normal displacement under different boundary conditions: (a) peak normal displacement; and (b) residual normal displacement.

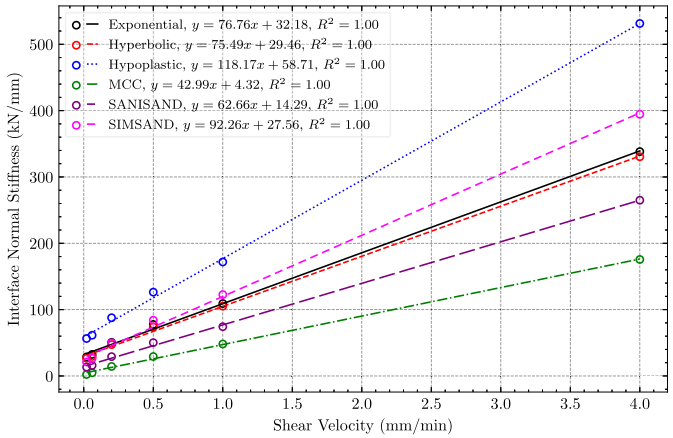

Fig. 16. Relationship between the normal stiffness and the shearing rate.

shear stress and normal displacement, which means that it successfully can predict only one variable under certain conditions. The results prove that the introduction of the dynamic peak stress ratio and dynamic phase transformation stress ratio is necessary for the simulation of the interface behaviors.

Effect of Shearing Velocity

The rate effect is another important aspect that should be considered in the interface modeling. Martinez and Stutz (2019) conducted a series of CNL experiments on a kaolin clay–steel interface with different shearing rates (Table 3). Martinez and Stutz (2019) observed that the interface transitions from a drained condition to a undrained condition with the increase of the shearing rate. Yang and Yin (2021) assumed the drained condition to be the CNL condition and the undrained condition to be the CV condition, considering the volumetric behaviors of these conditions based on experimental observations (Lemos and Vaughan 2000; Boukpeti and White 2017). The partially drained condition then was considered to be the CNS condition with different confining stiffness. Under the experimental CNL condition, the total normal stress remains constant, whereas the effective normal stress evolves differently due to variations in excess pore-water pressure generated at different shearing rates. Consequently, it is reasonable to assume that the boundary condition of the clay–structure interface shifts from the CNL condition to the CV condition as shearing rates increase. Nevertheless, it is not possible to simulate CNS or CV experiments with this assumption. Therefore, according to Yang and Yin (2021), the following assumptions can be made for clay–structure interface experiments with different shearing rates:

1. experiments with very low shearing rates involve a drained condition, and are considered to be CNL experiments;
2. experiments with very high shearing rates involve an undrained condition with no volumetric changes, and are considered to be CV experiments; and
3. experiments with medium shearing rates involve a partially drained condition, and are considered to be CNS experiments with different confining stiffness.

To determine the interface stiffness under different shearing rates, the objective function Eq. (35) is modified to consider the interface stiffness as calibrated parameters

$$\text{dist}[\mathbf{Y}^{\text{obs}}_{\tau|\sigma_n|u_n}, \mathbf{Y}^{\text{pre}}_{\tau|\sigma_n|u_n}(\mathbf{X},\mathbf{K})] = \sum_i l_i \left\| \frac{\mathbf{Y}^{\text{pre}}_i(\mathbf{X},\mathbf{K}) - \mathbf{Y}^{\text{obs}}_i}{\text{T}(\mathbf{Y}^{\text{obs}}_i)} \right\|, \quad i \in \{\tau, \sigma_n, u_n\} \tag{43}$$

where $\mathbf{K}$ is a vector of the interface normal stiffness corresponding to different shearing rates. The optimization-based parameter identification framework is used to identify the model parameters and the interface normal stiffness. Fig. 16 shows the relationship between the normal stiffness and the shearing rate. In Fig. 16, scatters represent calibrated interface normal stiffness, and lines represent the fitted relationship between the normal stiffness and the shearing rate. The normal stiffness increased linearly with the increase of the shearing rate. The normal stiffness was close to zero for normally consolidated clay experiments and overconsolidated clay experiments when the shearing rate was very small. The interface stiffness increased with the increase of the shearing rate. Thus, it is reasonable to assume that the interface changes from a drained condition to an undrained condition as it transitions from a CNL condition to a CV condition.

Models other than the MCC model do not consider the overconsolidation ratio. To simulate the overconsolidation effect, these models incorporate a density effect similar to that observed in sand, in which dense sand or overconsolidated clay exhibit dilative behavior during shearing, whereas loose sand or normally

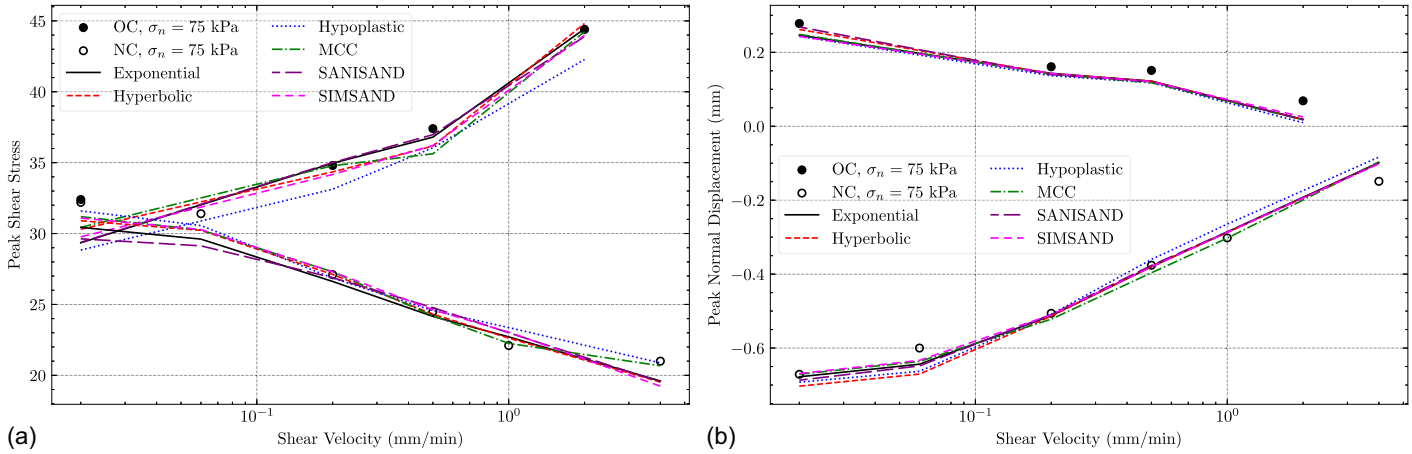

Fig. 17. Relationship between the peak shear stress/normal displacement and shearing velocity: (a) peak shear stress; and (b) peak normal displacement.

consolidated clay have contractive behavior. Fig. 17 shows the relationship between the peak shear stress or peak normal displacement and shearing velocity for normally consolidated clay and overconsolidated clay experiments. For normally consolidated clay, an increase in the shearing rate results in an decrease in the shear resistance and an increase in the volumetric change. For overconsolidated clay, an increase in the shearing rate results in an increase in the shear resistance and a decrease in the volumetric change. The results are consistent with the experimental observations of Martinez and Stutz (2019), as shown in Fig. 17. Furthermore, the preceding results show that all models are able of predicting the rate effect on the interface behaviors for both normally consolidated and overconsolidated clay–structure experiments. In the sand–structure interface experiments, the MCC model is not able to describe the tangential behavior and normal behavior simultaneously because the model does not consider the density-dependent interlocking and dilatancy effects. However, for the clay–structure interface experiments, the MCC model is able to describe the tangential behavior and normal behavior simultaneously, like other models. These results prove that in clay–structure interface experiments, the interlocking and dilatancy effect is not as important as in sand–structure interface experiments. Furthermore, the interlocking and dilatancy effect–related model parameters n_p and n_d in Table 5 are close to zero for the clay–structure interface experiments, which also confirms the preceding statement.

Conclusions

This paper evaluated the ability of six soil–structure interface models to simulate interface behaviors in order to guide users to choose a suitable model in specific conditions. Six soil–structure interface models were evaluated in this paper: the exponential model, the hyperbolic model, the hypoplastic model, the extended MCC model, the SANISAND model, and the SIMSAND model. An optimization-based parameter identification framework was introduced to identify the model parameters. Fontainebleau sand–steel interface experiments and kaolin clay–steel interface experiments were selected for the evaluation of the interface models. Model parameters were identified using the introduced optimization-based parameter identification framework.

These models were evaluated to identify the models' abilities to simulate the interface behaviors, including global comparisons, effect of soil relative density, interface stiffness, and shearing rate. Several different information criterion were used to select the preferred models for experiments under different conditions. It was found that the hypoplastic model is preferred for CNL experiments, the SANISAND model is preferred for CNS experiments under low confining pressure, and the exponential model is preferred for CNS experiments under high confining pressure. In general, nonlinear elastic models perform better than elastoplastic models. For the effect of soil relative density, it was found that the influence of the soil relative density on the exponential model and the SIMSAND model is greater than that of other models. An increase in the interface stiffness leads to an increase in the stress level for dense sand and to a decrease in the stress level for loose sand, due to the dilation of the dense sand and the contraction of the loose sand. The MCC model is not able to reproduce the alternating dilation and contraction behaviors that are observed in sand–steel interface experiments. The shearing rate effect can be simulated using different confining normal stiffness. The simulation results of the kaolin clay–steel interface experiments indicate that all models were able to simulate the clay–structure interface behaviors satisfactorily, even though the MCC model does not consider the density-dependent interlocking and dilatancy effects. In general, with the introduction of soil behaviors in simple nonlinear functions, nonlinear elastic models are able to simulate complex interface behaviors with simple formulations, and can do so better than complex elastoplastic models in some situations.

Data Availability Statement

All data of this study are available from the corresponding author upon reasonable request.

Acknowledgments

This research was financially supported by the Research Grants Council (RGC) of Hong Kong Special Administrative Region Government (HKSARG) of China (Grant No. 15217220, N_PolyU534/20).

References

Akaike, H. 1974. "A new look at the statistical model identification." *IEEE Trans. Autom. Control* 19 (6): 716–723. https://doi.org/10.1109/TAC.1974.1100705.

Arnold, M., and I. Herle. 2006. "Hypoplastic description of the frictional behaviour of contacts." In *Numerical methods in geotechnical engineering*, 101–106. New York: McGraw-Hill.

Boukpeti, N., and D. J. White. 2017. "Interface shear box tests for assessing axial pipe–soil resistance." *Géotechnique* 67 (1): 18–30. https://doi.org/10.1680/jgeot.15.P.112.

Brumund, W. F., and G. A. Leonards. 1973. "Experimental study of static and dynamic friction between sand and typical constuction materials." *J. Test. Eval.* 1 (2): 162–165. https://doi.org/10.1520/JTE10893J.

Clough, G. W., and J. M. Duncan. 1971. "Finite element analyses of retaining wall behavior." *ASCE J. Soil Mech. Found. Div.* 97 (12): 1657–1673. https://doi.org/10.1061/JSFEAQ.0001713.

DeJong, J. T., and Z. J. Westgate. 2009. "Role of initial state, material properties, and confinement condition on local and global soil-structure interface behavior." *J. Geotech. Geoenviron. Eng.* 135 (11): 1646–1660. https://doi.org/10.1061/(ASCE)1090-0241(2009)135:11(1646).

DeJong, J. T., D. J. White, and M. F. Randolph. 2006. "Microscale observation and modeling of soil-structure interface behavior using particle image velocimetry." *Soils Found.* 46 (1): 15–28. https://doi.org/10.3208/sandf.46.15.

Desai, C. S., E. C. Drumm, and M. M. Zaman. 1985. "Cyclic testing and modeling of interfaces." *J. Geotech. Eng.* 111 (6): 793–815. https://doi.org/10.1061/(ASCE)0733-9410(1985)111:6(793).

Desai, C. S., and Y. Z. Ma. 1992. "Modeling of joints and interfaces using the disturbed-state concept." *Int. J. Numer. Anal. Methods Geomech.* 16 (9): 623–653. https://doi.org/10.1002/nag.1610160903.

Desai, C. S., and D. B. Rigby. 1997. "Cyclic interface and joint shear device including pore pressure effects." *J. Geotech. Geoenviron. Eng.* 123 (6): 568–579. https://doi.org/10.1061/(ASCE)1090-0241(1997)123:6(568).

Di Donna, A., A. Ferrari, and L. Laloui. 2016. "Experimental investigations of the soil–concrete interface: Physical mechanisms, cyclic mobilization, and behaviour at different temperatures." *Can. Geotech. J.* 53 (4): 659–672. https://doi.org/10.1139/cgj-2015-0294.

Duque, J., M. Yang, W. Fuentes, D. Mašín, and M. Taiebat. 2022. "Characteristic limitations of advanced plasticity and hypoplasticity models for cyclic loading of sands." *Acta Geotech.* 17 (6): 2235–2257. https://doi.org/10.1007/s11440-021-01418-z.

Fakharian, K., and E. Evgin. 1997. "Cyclic simple-shear behavior of sand-steel interfaces under constant normal stiffness condition." *J. Geotech. Geoenviron. Eng.* 123 (12): 1096–1105. https://doi.org/10.1061/(ASCE)1090-0241(1997)123:12(1096).

Fakharian, K., and E. Evgin. 2000. "Elasto-plastic modelling of stress-path-dependent behaviour of interfaces." *Int. J. Numer. Anal. Methods*

Geomech. 24 (2): 183–199. https://doi.org/10.1002/(SICI)1096-9853(200002)24:2<183::AID-NAG63>3.0.CO;2-3.

Gu, X., Y. Chen, and M. Huang. 2017. "Critical state shear behavior of the soil–structure interface determined by discrete element modeling." *Particuology* 35 (Dec): 68–77. https://doi.org/10.1016/j.partic.2017.02.002.

Hansen, N. 2023. "CMA-ES/pycma: r3.3.0." Accessed January 26, 2023. https://doi.org/10.5281/zenodo.7573532.

Hansen, N. 2016. "The CMA evolution strategy: A tutorial." Preprint, submitted April 4, 2016. https://arxiv.org/abs/1604.00772.

Hansen, N., and A. Ostermeier. 1996. "Adapting arbitrary normal mutation distributions in evolution strategies: The covariance matrix adaptation." In *Proc., IEEE Int. Conf. on Evolutionary Computation*, 312–317. New York: IEEE.

Hardin, B. O. 1985. "Crushing of soil particles." *J. Geotech. Eng.* 111 (10): 1177–1192. https://doi.org/10.1061/(ASCE)0733-9410(1985)111:10(1177).

Ho, T., R. Jardine, and N. Anh-Minh. 2011. "Large-displacement interface shear between steel and granular media." *Géotechnique* 61 (3): 221–234. https://doi.org/10.1680/geot.8.P.086.

Hu, L. M., and J. L. Pu. 2004. "Testing and modeling of soil-structure interface." *J. Geotech. Geoenviron. Eng.* 130 (8): 851–860. https://doi.org/10.1061/(ASCE)1090-0241(2004)130:8(851).

Hurvich, C. M., and C.-L. Tsai. 1989. "Regression and time series model selection in small samples." *Biometrika* 76 (2): 297–307. https://doi.org/10.1093/biomet/76.2.297.

Jin, Y.-F., Z.-Y. Yin, Z.-X. Wu, and A. Daouadji. 2018. "Numerical modeling of pile penetration in silica sands considering the effect of grain breakage." *Finite Elem. Anal. Des.* 144 (May): 15–29. https://doi.org/10.1016/j.finel.2018.02.003.

Kishida, H., and M. Uesugi. 1987. "Tests of the interface between sand and steel in the simple shear apparatus." *Géotechnique* 37 (1): 45–52. https://doi.org/10.1680/geot.1987.37.1.45.

Knabe, T., H. F. Schweiger, and T. Schanz. 2012. "Calibration of constitutive parameters by inverse analysis for a geotechnical boundary problem." *Can. Geotech. J.* 49 (2): 170–183. https://doi.org/10.1139/t11-091.

Kohavi, R. 1995. "A study of cross-validation and bootstrap for accuracy estimation and model selection." In Vol. 2 of *Proc., 14th Int. Joint Conf. on Artificial Intelligence—IJCAI'95*, 1137–1143. San Francisco: Morgan Kaufmann Publishers.

Koval, G., F. Chevoir, J. N. Roux, J. Sulem, and A. Corfdir. 2011. "Interface roughness effect on slow cyclic annular shear of granular materials." *Granular Matter* 13 (5): 525–540. https://doi.org/10.1007/s10035-011-0267-2.

Lashkari, A. 2013. "Prediction of the shaft resistance of nondisplacement piles in sand." *Int. J. Numer. Anal. Methods Geomech.* 37 (8): 904–931. https://doi.org/10.1002/nag.1129.

Lemos, L. J. L., and P. R. Vaughan. 2000. "Clay–interface shear resistance." *Géotechnique* 50 (1): 55–64. https://doi.org/10.1680/geot.2000.50.1.55.

Littleton, I. 1976. "An experimental study of the adhesion between clay and steel." *J. Terramech.* 13 (3): 141–152. https://doi.org/10.1016/0022-4898(76)90003-3.

Martinez, A., and J. D. Frost. 2017. "The influence of surface roughness form on the strength of sand– structure interfaces." *Géotech. Lett.* 7 (1): 104–111. https://doi.org/10.1680/jgele.16.00169.

Martinez, A., and H. H. Stutz. 2019. "Rate effects on the interface shear behaviour of normally and overconsolidated clay." *Géotechnique* 69 (9): 801–815. https://doi.org/10.1680/jgeot.17.P.311.

Mortara, G. 2001. "An elastoplastic model for sand-structure interface behaviour under monotonic and cyclic loading." Ph.D. thesis, Dept. of Structural, Geotechnical and Building Engineering, Politecnico di Torino.

O'Rourke, T. D., S. J. Druschel, and A. N. Netravali. 1990. "Shear strength characteristics of sand-polymer interfaces." *J. Geotech. Eng.* 116 (3): 451–469. https://doi.org/10.1061/(ASCE)0733-9410(1990)116:3(451).

Potyondy, J. G. 1961. "Skin friction between various soils and construction materials." *Géotechnique* 11 (4): 339–353. https://doi.org/10.1680/geot.1961.11.4.339.

Pra-Ai, S. 2013. "Behaviour of soil–structure interfaces subjected to large number of cycles. Application to piles." Ph.D. thesis, École doctorale Ingénierie - Matériaux, Mécanique, Environnement, Énergétique, Procédés, Production (I-MEP2), Université de Grenoble.

Qamar, M. I. A., and M. T. Suleiman. 2023. "Development of cyclic interface shear test device and testing procedure to measure the response of cohesive soil-structure interface." *Geotech. Test. J.* 46 (3): 488–509. https://doi.org/10.1520/GTJ20210270.

Richart, F. E., J. R. Hall, and R. D. Woods. 1970. *Vibrations of soils and foundations*. Upper Saddle River, NJ: Prentice Hall.

Roscoe, K., and JB. Burland. 1968. *On the generalized stress-strain behaviour of wet clay.* Cambridge, UK: Cambridge University Press.

Schwarz, G. 1978. "Estimating the dimension of a model." *Ann. Stat.* 6 (2): 461–464. https://doi.org/10.1214/aos/1176344136.

Staubach, P., J. Machaček, and T. Wichtmann. 2022a. "Mortar contact discretisation methods incorporating interface models based on hypoplasticity and Sanisand: Application to vibratory pile driving." *Comput. Geotech.* 146 (Jun): 104677. https://doi.org/10.1016/j.compgeo.2022.104677.

Staubach, P., J. Machaček, and T. Wichtmann. 2022b. "Novel approach to apply existing constitutive soil models to the modelling of interfaces." *Int. J. Numer. Anal. Methods Geomech.* 46 (7): 1241–1271. https://doi.org/10.1002/nag.3344.

Stutz, H. 2016. "Hypoplastic models for soil–structure interfaces: Modelling and implementation." Ph.D. thesis, Faculty of Mathematics and Natural Sciences, Kiel Univ.

Stutz, H., D. Masin, and F. Wuttke. 2016. "Enhancement of a hypoplastic model for granular soil–structure interface behaviour." *Acta Geotech.* 11 (6): 1249–1261. https://doi.org/10.1007/s11440-016-0440-1.

Stutz, H., D. Mašín, A. S. Sattari, and F. Wuttke. 2017. "A general approach to model interfaces using existing soil constitutive models application to hypoplasticity." *Comput. Geotech.* 87 (Jul): 115–127. https://doi.org/10.1016/j.compgeo.2017.02.010.

Stutz, H., G. Mortara, and F. Wuttke. 2015. "Simple vs advanced interface model: A comparison using a deterministic quality approach." In *Deformation characteristics of geomaterials*, 1105–1112. Amsterdam, Netherlands: IOS Press.

Taha, A., and M. Fall. 2013. "Shear behavior of sensitive marine clay-concrete interfaces." *J. Geotech. Geoenviron. Eng.* 139 (4): 644–650. https://doi.org/10.1061/(ASCE)GT.1943-5606.0000795.

Taiebat, M., and Y. F. Dafalias. 2008. "SANISAND: Simple anisotropic sand plasticity model." *Int. J. Numer. Anal. Methods Geomech.* 32 (8): 915–948. https://doi.org/10.1002/nag.651.

Tovar-Valencia, R. D., A. Galvis-Castro, R. Salgado, and M. Prezzi. 2018. "Effect of surface roughness on the shaft resistance of displacement model piles in sand." *J. Geotech. Geoenviron. Eng.* 144 (3): 04017120. https://doi.org/10.1061/(ASCE)GT.1943-5606.0001828.

Tsubakihara, Y., and H. Kishida. 1993. "Frictional behaviour between normally consolidated clay and steel by two direct shear type apparatuses." *Soils Found.* 33 (2): 1–13. https://doi.org/10.3208/sandf1972.33.2_1.

Uesugi, M., and H. Kishida. 1986. "Frictional resistance at yield between dry sand and mild steel." *Soils Found.* 26 (4): 139–149. https://doi.org/10.3208/sandf1972.26.4_139.

Uesugi, M., H. Kishida, and Y. Tsubakihara. 1988. "Behavior of sand particles in sand–steel friction." *Soils Found.* 28 (1): 107–118. https://doi.org/10.3208/sandf1972.28.107.

Wang, S., W. Wu, Z.-Y. Yin, C. Peng, and X. He. 2018. "Modelling the time-dependent behaviour of granular material with hypoplasticity." *Int. J. Numer. Anal. Methods Geomech.* 42 (12): 1331–1345. https://doi.org/10.1002/nag.2793.

Wernick, E. 1978. "Skin friction of cylindrical anchors in non-cohesive soils." In *Proc., Symp. on Soil Reinforcing and Stabilising Techniques*, 201–219. Sydney, Australia: New South Wales Institute of Technology.

Yang, D., S. Niu, Y. Cai, W. Feng, and D. Zhang. 2021. "Analysis of shear characteristics of cohesive soil and rigid base: A case study of concrete base." *Geotech. Geol. Eng.* 39 (1): 135–143. https://doi.org/10.1007/s10706-020-01478-0.

Yang, J., and Z.-Y. Yin. 2021. "Soil-structure interface modeling with the nonlinear incremental approach." *Int. J. Numer. Anal. Methods Geomech.* 45 (10): 1381–1404. https://doi.org/10.1002/nag.3206.

Yasufuku, N., and H. Ochiai. 2005. *Sand–steel interface friction related to soil crushability. Geotechnical special publication*, 627–641. Reston, VA: ASCE.

Yasufuku, N., H. Ochiai, and T. Kaku. 2003. "Internal friction of sand along steel surface up to an interfacial critical state." [In Japanese.] *J Appl Mech* 6 (Aug): 563–571. https://doi.org/10.2208/journalam.6.563.

Yavari, N., A. M. Tang, J. M. Pereira, and G. Hassen. 2016. "Effect of temperature on the shear strength of soils and the soil–structure interface." *Can. Geotech. J.* 53 (7): 1186–1194. https://doi.org/10.1139/cgj-2015-0355.

Yin, K., A.-L. Fauchille, E. Di Filippo, P. Kotronis, and G. Sciarra. 2021. "A review of sand–clay mixture and soil–structure interface direct shear test." *Geotechnics* 1 (2): 260–306. https://doi.org/10.3390/geotechnics1020014.

Yin, Z.-Y., and C. S. Chang. 2013. "Stress–dilatancy behavior for sand under loading and unloading conditions." *Int. J. Numer. Anal. Methods Geomech.* 37 (8): 855–870. https://doi.org/10.1002/nag.1125.

Yin, Z.-Y., H.-W. Huang, and P.-Y. Hicher. 2016. "Elastoplastic modeling of sand–silt mixtures." *Soils Found.* 56 (3): 520–532. https://doi.org/10.1016/j.sandf.2016.04.017.

Yin, Z.-Y., Z.-X. Wu, and P.-Y. Hicher. 2018. "Modeling monotonic and cyclic behavior of granular materials by exponential constitutive function." *J. Eng. Mech.* 144 (4): 04018014. https://doi.org/10.1061/(ASCE)EM.1943-7889.0001437.

Yoshimi, Y., and T. Kishida. 1981. "A ring torsion apparatus for evaluating friction between soil and metal surfaces." *Geotech. Test. J.* 4 (4): 145–152. https://doi.org/10.1520/GTJ10783J.

Zhang, G., and J.-M. Zhang. 2006. "Large-scale apparatus for monotonic and cyclic soil–structure interface test." *Geotech. Test. J.* 29 (5): 401–408. https://doi.org/10.1520/GTJ100225.

Zhou, W.-H., and Z.-Y. Yin. 2023. *Practice of discrete element method in soil–structure interface modelling*. Singapore: Springer Nature.